



Multi-material topology optimization and additive manufacturing for metamaterials incorporating double negative indexes of Poisson's ratio and thermal expansion

Zhengtong Han, Kai Wei*

State Key Laboratory of Advanced Design and Manufacturing for Vehicle Body, Hunan University, Changsha 410082, PR China

ARTICLE INFO

Keywords:

Metamaterial
Topology optimization
Multi-material additive manufacturing
Fused Deposition Modeling
Poisson's ratio
Thermal expansion

ABSTRACT

Advances in the multi-material additive manufacturing promote a new opportunity for developing metamaterials integrating complex functionalities, especially the metamaterial incorporating double negative indexes of Poisson's ratio and thermal expansion. However, the systematic design and additive manufacturing of such metamaterial are stilling not developed. Here, an improved multi-material topology optimization method, Alternating Active Phase & Objective (AAPO) algorithm, was developed. A new optimization formulation, in which the core contribution was the dynamical switch of the objective functions according to the active phases, was proposed to successfully overcome the convergence oscillation. The optimization formulation and sensitivity analysis based on the numerical homogenization were established. A series of multi-material re-entrant and chiral metamaterials, which exclusively realized the double negative indexes of Poisson's ratio and thermal expansion, were devised. Especially, the tri-material and chiral metamaterials were originally obtained through the topology optimization. More importantly, metamaterials were well additively manufactured through the multi-material fused deposition modeling. The experimentally tested Poisson's ratio and thermal expansion suggest a good agreement between the experiments and topology-optimized results. The multi-material design and additive manufacturing developed here provide a general guidance to develop the multi-functional metamaterials.

1. Introduction

The design of the mechanical metamaterial which features counter-intuitive functions, such as the negative Poisson's ratio (PR) [1], negative compressibility [2,3] and negative coefficient of thermal expansion (CTE) [4], etc., has attracted enormous attention in recent years [5]. In particular, metamaterials with negative PR expand laterally when they are stretched and vice versa. This distinctive function is beneficial to strengthen the crack resistance [6], fracture toughness [7] and sound absorption capacity [8]. Various metamaterials with different deformation mechanisms have been devised to solely present the negative PRs, including the re-entrant type [9–11], chiral type [12–14] and rotating type [15], etc. Similarly, CTE is an important thermal parameter, which measures the dimensional variation under a temperature increment. Metamaterials with negative CTE are urgently needed in aerospace structures, precision instruments and electronic equipment in order to purposely modulate their thermal expansions [16]. Typical

metamaterials, which solely give the negative CTEs, can be classified into the bend-dominated [17–20] and stretch-dominated [21–23] types as discussed in Ref. [20].

Compared with the metamaterials which just can give either negative PR or negative CTE, multi-functional metamaterials could offer the promising ability to increase their efficiency and practicability [24]. From the practical views of point, metamaterials incorporating double negative indexes of PR and CTE will provide much more design margin for both mechanical- and temperature-sensitive devices widely used in the satellites and aircrafts [25,26]. However, up to now, only a few works reported such kind of multi-functional metamaterials which were classified into re-entrant type [16,27–31] and chiral type [32–35] according to their basic geometrical feature [5]. As illustrated in Fig. 1(a), the underlying design rule in these works can be classified as a 'direct design' principle. These metamaterials are designed strongly relying on the individual intuition and experience in architected or cellular materials. Then, complex theoretical deduction and parameter analysis

* Corresponding author.

E-mail address: weikai@hnu.edu.cn (K. Wei).

<https://doi.org/10.1016/j.addma.2022.102742>

Received 2 December 2021; Received in revised form 20 February 2022; Accepted 7 March 2022

Available online 12 March 2022

2214-8604/© 2022 Elsevier B.V. All rights reserved.

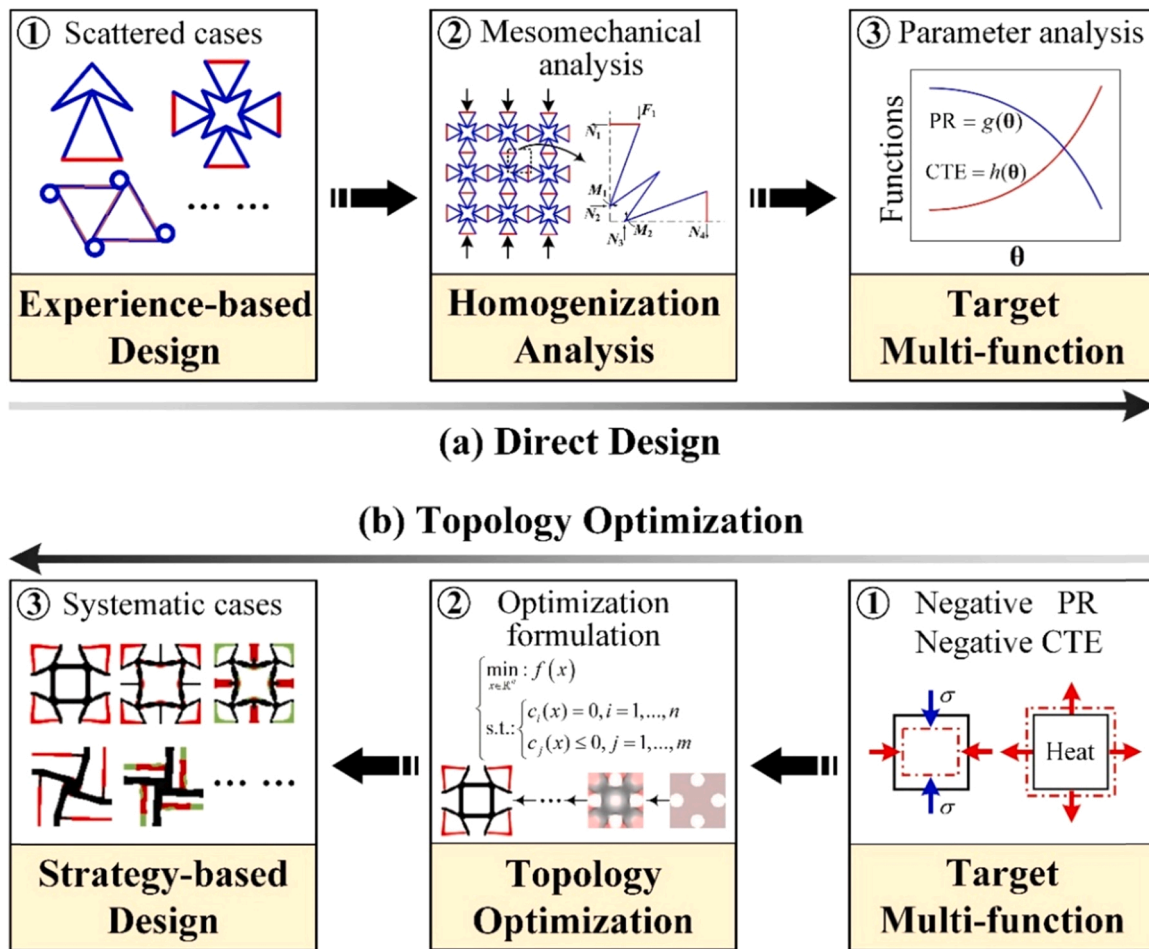


Fig. 1. (a): In the direct design, scattered metamaterials are designed and analyzed strongly relying on the individual intuition and experience. (b): Topology optimization, as an inverse homogenization procedure, provides a rigorous framework for designing systematical metamaterials, once the target functions are pre-determined.

Table 1
List of multi-material topology optimization algorithms in literature.

| Classification | | Material interpolation | Remarks |
|-----------------------------------|---|---|--|
| Homogenization/SIMP-based method | SIMP, 1999 [39] | 2 materials: $E(\rho) = \rho_1^{\beta_1} (\rho_2^{\beta_2} E_1 + (1 - \rho_2^{\beta_2}) E_2)$ N materials: formulation is too complex | Multi-materials resulted in a complex interpolation expression |
| | Peak function interpolation, 2001 [40] | $E(\rho) = \sum_{i=1}^N E_i \exp \left[\frac{(\rho - \mu_i)^2}{(2\sigma_i^2)} \right]$ | The zero slope of the interpolation resulted in the difficulty of the numerical calculation |
| | Alternating active-phase method, 2014 [41] Ordered SIMP, 2017 [42] | $+E_{\text{void}}$ Power-law interpolation used in the SIMP method Ordered SIMP interpolation | Generality, simplicity and insensitivity to material numbers but a considerable computational cost Generalized for any material without increasing the computational cost |
| BESO method | An improved SIMP, 2018 [43] | Power-law interpolation used in the SIMP method with reciprocal variables | Multi-materials resulted in a complex interpolation expression |
| | BESO, 2009 [44] | Power-law interpolation used in the SIMP method | Hard to solve problems with multiple constraints |
| | An improved BESO, 2015 [45] | Power-law interpolation used in the SIMP method | |
| Level set method | Vector level set, 2004 [46] | A set of Hamilton–Jacobi PDEs | Multi-materials resulted in a complex interpolation expression |
| Combinatorial optimization method | Pseudo-sensitivity based method, 2010 [47] | Discrete variables | Pseudo-sensitivity decreases the accuracy |
| | ZPR, 2018 [48] | Discrete material interpolation | No limits on the number of candidate materials, but a high computational cost |

should be mandatorily performed to figure out whether the target functions can be obtained. The inherent major deficiency caused by this design procedure is that only the scattered designs could be found with a low design efficiency, resulting in an obvious restriction to the further

development of novel metamaterials [36].

Differently, in Fig. 1(b), metamaterials can be systematically designed by an inverse homogenization procedure using topology optimization [37,38]. As a function-driven strategy, the target multiple

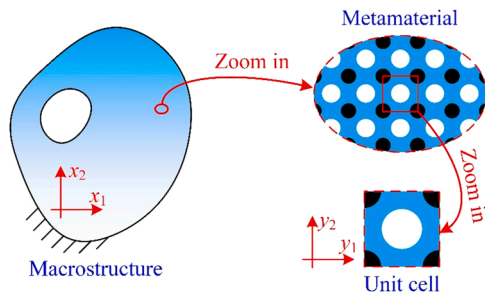


Fig. 2. Principle for introducing numerical homogenization method: The macrostructure is consisted of the metamaterial which includes the unit cells. The different colors represent different base materials.

functions are defined beforehand. Then the topological configurations are generally searched through the topology optimization formulation to fulfill the pre-defined target multiple functions. It provides a rigorous framework for generating systematical multi-functional metamaterials, once the target functions are pre-determined.

Benefited from the topology optimization, various metamaterials with either negative PR or negative CTE have been designed. For the former one, O. Sigmund adopted the Solid Isotropic Material with Penalization (SIMP) method to design specified metamaterials with negative PR [49]. Subsequently, this method was extended to tailor the auxetic metamaterial with introducing the bi-material topology optimization [50], nonlinear homogenization [51], isogeometric analysis [52], etc. As for the metamaterials with negative CTE, it could be realized only through constructing two different base materials with different positive CTEs [53,54], and thus a multi-material topology optimization is mandatorily required. As summarized in Table 1, these algorithms can be classified as the SIMP-based, BESO-based, level set-based and combinatorial optimization-based. More discussion on their advantages and disadvantages can be found in Ref. [55]. Typically, O. Sigmund et al. [53,54] designed such kind of metamaterials through the bi-material SIMP method. M. Hirota and Y. Kanno [56] refined the frame structural optimization problem as a mixed-integer linear programming (MILP) problem and obtained the negative CTE metamaterials. A. Takezawa et al. [57] developed a methodology for designing porous metamaterials with arbitrary CTE using a SIMP-based bi-material topology optimization.

However, few works aimed at designing the metamaterials with both indexes of PR and CTE through the topology optimization. To our best knowledge, only Y. Wang et al. [58] designed re-entrant metamaterials with desired PR and CTE, suggesting that the topology optimization of multi-functional metamaterials is still in its infancy. From the perspective of the basic topological configuration, only re-entrant metamaterials were topologically optimized, ignoring the fact that metamaterials with chiral feature are also of great importance. Besides, increasing the number of the different base materials to enhance the metamaterial performance has attracted much attention in the direct designs. M.M. Chen [28] developed a triangular metamaterial composed of three base materials that can effectively increase the thermal expansion control range. M.H. Fu proposed [35] a new tri-material three-dimensional metamaterial with a large range of CTEs. In comparison, the material variety of the metamaterial topology optimization is still constrained within only two base materials (not containing void phase), inherently limiting the design space.

Among the algorithms listed in Table 1, the Alternating Active Phase (AAP) algorithm proposed by R. Tavakoli and S.M. Mohseni [41] was found to have a great potential of which the detail information is introduced in Appendix A. In brief, during the algorithm processing, a multi-material topology optimization problem is converted into a series of traditional binary-phase (solid-void phase) topology optimization sub-problems which can be solved easily. Due to its generality,

simplicity, insensitivity to material numbers and ease of implementation, the AAP algorithm and several improved versions, which include algorithms unified with meshless method [59], isogeometric analysis [60] and level set method [61], has been applied successfully in a wide range of structural designs including three-dimensional problems [62], stress constrains problems [55] and compliant mechanisms [63]. However, using the AAP algorithm to design metamaterial has not been reported yet.

Indeed, implementing the original AAP into designing the multi-functional metamaterials is still challenging, in part, due to the contradiction between the objective function and combination of the active phases. All the previous topology optimization works [58,64] for multi-functional metamaterials were based on a weighted sums method [65] where the original multiple functions were combined into one according to the artificially pre-defined weights. Unfortunately, this method would degenerate the sub-problems in the AAP algorithm into a single material topology optimization problem when one of the active phases is void. In this situation, the optimization of the CTE cannot be proceeded, resulting in the oscillatory behavior in the combined objective function. Another critical challenge is related to the potential instability in convergence. Previous studies on macrostructures [41,61] revealed that some controlling parameters, such as the maximum number of each sub-problem, presented significant influence on the performance of the AAP algorithm. The proper ranges of these controlling parameters are unknown beforehand, leading to another serious obstacle to extending the AAP algorithm into designing the multi-functional metamaterials.

The main intention of this work is to extend the AAP algorithm into designing the multi-functional metamaterials. The main contributions were: (a) An Alternating Active Phase & Objective algorithm (AAPO) was successfully developed to design the multi-functional metamaterial, in which the objective functions switch dynamically between the loops according to the material distribution; (b) The universality of the controlling parameters in the AAPO algorithm was identified to ensure the robustness and convergence; (c) A series of multi-material (bi-material and tri-material, both not containing void phase) re-entrant and chiral metamaterials, which exclusively realized double negative indexes of Poisson's ratio and thermal expansion, were successfully designed. Especially, the tri-material ones and chiral ones were obtained through topology optimization for the first time; (d) The underlying mechanisms of the double negative indexes in these metamaterials were originally revealed, providing a guideline to integrate the negative Poisson's ratio and negative thermal expansion. (e) Using multi-material additive manufacturing, the metamaterials were practically fabricated and experimentally measured to firmly demonstrate the effectiveness of the proposed AAPO algorithm.

The remainder of this work is organized as follows: In Section 2, the Alternating Active Phase & Objective (AAPO) algorithm is developed. In Section 3, five numerical examples are discussed to demonstrate the effectiveness of the proposed algorithm. The numerical verification and the underlying deformation mechanisms of the obtained metamaterials are analyzed in detail. Multi-material additive manufacturing and physical experiments are presented in Section 4 and the conclusion is drawn in Section 5. The information of the basic AAP algorithm and the derivation of the sensitivity information are given in Appendix A and B, respectively.

2. Alternating active phase and objective algorithm

This work aims to solve the topology optimization of multi-material metamaterials for purpose of integrating both the extremely negative PR and negative CTE based on the AAP algorithm. In order to emphasize the main contribution of this work, the basic introduction of the AAP algorithm is described in Appendix A. Overall, incorporating the weighted sums method, which was developed to satisfy the multi-functional requirement [57,58], into the AAP algorithm will lead to the

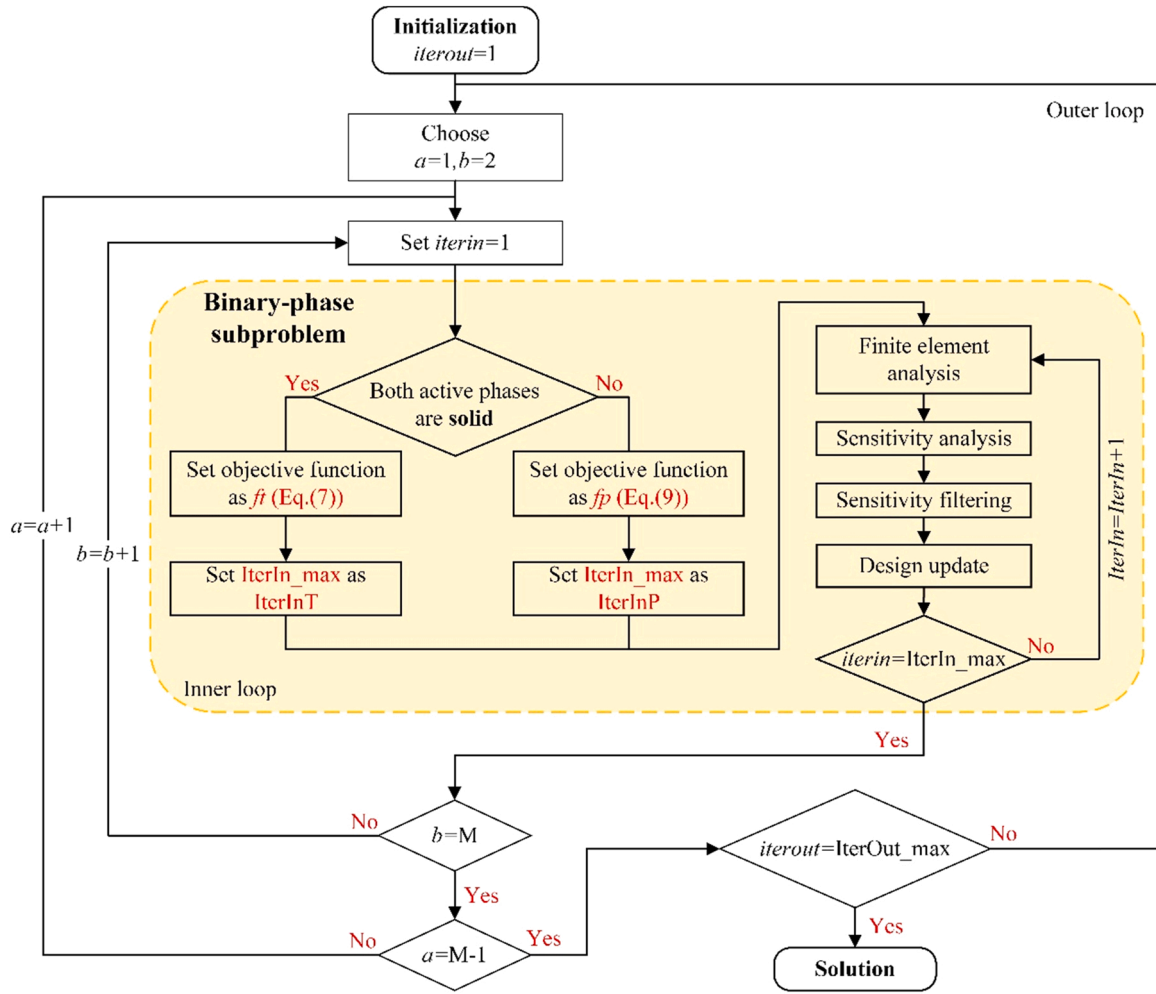


Fig. 3. Flow chart of the Alternating Active Phase & Objective algorithm.

oscillatory behavior in the convergence. Accordingly, herein, a new optimization formulation is originally proposed, and the computational stability are significantly ensured.

2.1. Numerical homogenization method

The design of multi-functional metamaterials in this work is based on the asymptotic homogenization (AH) method, which is used to determine the effective properties of the metamaterial [66]. As shown in Fig. 2, this analysis is performed on a unit cell: the smallest representative volume element in a metamaterial. There are two basic assumptions should be fulfilled:

- (1) Field quantities, such as displacement and strain, depend on two different scales: One on the macroscopic level x , and the other on the microscopic level $y = x/\epsilon$, ϵ is a magnification factor that scales the dimensions of the unit cell to the dimensions of the macrostructure.
- (2) Field quantities vary smoothly at the macroscopic level: The unit cell needs to be periodically patterned in the metamaterial.

Then, a two-dimensional square with two or more base materials is defined as the design domain. For a linear elastic material, the displacement field χ^ϵ at the macrostructure can be written as an asymptotic expansion:

$$\chi^\epsilon(\mathbf{x}) = \chi_0(\mathbf{x}, \mathbf{y}) + \epsilon \chi_1(\mathbf{x}, \mathbf{y}) + \epsilon^2 \chi_2(\mathbf{x}, \mathbf{y}) + \dots \quad (1)$$

where \mathbf{x} and \mathbf{y} are macroscopic and microscopic (unit cell) coordinates, respectively. ϵ is the aspect ratio between the two scales and is far less than 1. For numerical simplicity, only the first-order term is considered, and the effective elastic tensor C^H , which describes the macroscopic behavior of the periodic unit cells, is written as:

$$C_{ijkl}^H = \frac{1}{|Y|} \int_Y [\epsilon_{pq}^{0(ij)} - \epsilon_{pq}^*(\chi^{ij})] C_{pqrs} [\epsilon_{rs}^{0(kl)} - \epsilon_{rs}^*(\chi^{kl})] dY \quad (2)$$

where $|Y|$ is the volume of the unit cell. C_{pqrs} is the elasticity tensor. $\epsilon_{pq}^{0(ij)}$ are the applied macroscopic unit fields in a planar problem: the horizontal unit strain is the unit test field $\epsilon_{pq}^{0(11)} = [1 \ 0 \ 0]$, the vertical unit strain is $\epsilon_{pq}^{0(22)} = [0 \ 1 \ 0]$ and the shear unit strain is $\epsilon_{pq}^{0(12)} = [0 \ 0 \ 1]$. τ_{pq} is the applied thermal load. $\epsilon_{rs}^*(\chi^{kl})$ represents the locally varying strain field with the loading case kl . Similarly, the thermal expansion characteristics of the unit cell can be homogenized. The effective thermal stress tensor β^H is:

$$\beta_{pq}^H = \frac{1}{|Y|} \int_Y [\tau_{pq} - \epsilon_{pq}^*(\psi)] - C_{pqkl} [\epsilon_{kl}^{0(ij)} - \epsilon_{kl}^*(\chi^{kl})] dY \quad (3)$$

where $\epsilon_{pq}^*(\psi)$ is the strain field based on the displacement field for a unit thermal load. Thus, the effective thermal expansion tensor α^H can be calculated as:

$$\alpha_{ij}^H = (C_{ijpq}^H)^{-1} \beta_{pq}^H \quad (4)$$

Table 2
Materials and corresponding properties used in the numerical examples.

| Numerical example | Material | Young's modulus | Coefficient of thermal expansion | Poisson's ratio | Volume constraint |
|-------------------|----------|-----------------|----------------------------------|-----------------|-------------------|
| 1,3 | Mat-1 | 1 | 1 | 0.3 | 0.2 |
| | Mat-2 | 1 | 10 | 0.3 | 0.1 |
| 2 | Mat-1 | 10 | 2 | 0.3 | 0.2 |
| | Mat-2 | 2 | 10 | 0.3 | 0.1 |
| 4, 5 | Mat-1 | 10 | 2 | 0.3 | 0.2 |
| | Mat-2 | 2 | 10 | 0.3 | 0.1 |
| | Mat-3 | 1 | 20 | 0.3 | 0.1 |

The displacement fields χ^{kl} and ψ can be obtained by solving the problem over the unit cell:

$$\int_Y \left[\varepsilon_{pq}^{0(kl)} - \varepsilon_{pq}^*(\chi^{kl}) \right] C_{pqrs} \varepsilon_{rs}(v) dY = 0 \quad (5)$$

$$\int_Y \left[\tau_{pq} - \varepsilon_{pq}^*(\psi) \right] C_{pqrs} \varepsilon_{rs}(v) dY = 0 \quad (6)$$

where v is the virtual displacement field.

2.2. Optimization formulation of AAPO algorithm

Different from the original AAP algorithm, in addition to the dynamically adjusted active phases, the objective functions also switch between the loops according to the combination of the active phases. In detail, the negative CTE in a metamaterial can only be obtained through integrating at least two or more solid base materials with different positive CTEs. For an arbitrary sub-problem built in the AAPO, if the active phases are all solid, the objective function is set to achieve the negative CTE:

$$\min : ft = \sum_{ij}^d \alpha_{ij}^H \quad (7)$$

To control the iterative number, a parameter IterInT is introduced to limit the maximum iterative number. Otherwise, for an arbitrary sub-problem, if one of the active phases is void, the objective function is set to optimize the negative PR. The PR in two orthotropic directions of a two-dimensional metamaterials can be defined as: $\nu_{12} = C_{12}^H/C_{11}^H$ and $\nu_{21} = C_{12}^H/C_{22}^H$. C^H represents the effective elasticity tensor which can be written in the following matrix for a two-dimensional problem [67]:

$$C^H = \begin{bmatrix} C_{11} & C_{12} & C_{13} \\ & C_{22} & C_{23} \\ \text{Syms} & & C_{33} \end{bmatrix} \quad (8)$$

In previous works, several objective functions have been proposed to generate such auxetic effect such as the minimization of the difference between the predicted negative PR and its target [68], the minimization of the weighted square difference between the effective tensor and expected elastic tensor [69] and the minimization of a relaxed combination of the effective elastic tensor [50]. Here, the last kind of the objective function is selected, and it is written as:

$$\min : fp = C_{12}^H - \lambda^l (C_{11}^H + C_{22}^H) \quad (9)$$

where λ is a fixed parameter which is defined as 0.8 according to Ref. [50]. l is the iteration number which is equal to the number of the outer loop. The advantage of such a kind of objective function is that the stiffness in the principal directions can be guaranteed, since the terms C_{11}^H and C_{22}^H will always be involved in the objective function. Another parameter IterInP is introduced to control the iterative number of this subproblem.

Finally, the optimization formulation of the multi-functional topol-

ogy optimization problem is established as:

$$\begin{aligned} & \text{Find : } \rho_{ea} (e \in \mathbf{Ne}) \\ & \min : f(\boldsymbol{\rho}) = \text{fitofp} \\ & \text{s.t. : } \left\{ \begin{aligned} & f_v(\boldsymbol{\rho}) = \sum_{e \in \mathbf{Ne}} \rho_{ea}(\mathbf{x}) v_e - V_a^* \leq 0 \quad 0 \leq \rho_{ea} \leq 1, e \in \mathbf{Ne} \end{aligned} \right. \end{aligned} \quad (10)$$

The flow chat of the proposed AAPO algorithm is illustrated in Fig. 3. The algorithm starts from selecting two active phases represented by 'a' and 'b'. Then, a sub-problem consisting of these two phases is built through the SIMP-based method. During the updating process, the objective function of the sub-problem and maximum number of the inner loop (IterIn_max) varies along with the active phases. If one of the active phases is void, this sub-problem is built to achieve the extremely negative PR according to Eq., since its CTE cannot be optimized. The IterIn_max is set to be IterInP. On the other hand, if both active phases are solid, the sub-problem is built to achieve the extremely negative CTE according to Eq. The IterIn_max needs to be set to be IterInT. The topology optimization process will be terminated, when the maximum iteration number of the outer loop (IterOut_max) is reached.

Compared with the original AAP algorithm demonstrated in Fig. A1, the optimization process can be stably solved, since the void phase is excluded along with the dynamically switched objective function. Thus, the high convergence oscillation arisen from the weighted sums method in each sub-problem can be effectively eliminated.

3. Numerical examples

In this section, five numerical examples are performed to demonstrate the effectiveness of the AAPO algorithm. The design domain corresponds to a square with periodic boundary conditions, and plane stress condition are applied. Firstly, the influences of the controlling parameters, IterInT and IterInP introduced in Section 2, on the topology optimization results were studied. Their appropriate ranges were identified through systematic discussion in the first three numerical examples. Then, the topology optimization of tri-material multi-functional metamaterials, which has not been reported yet, was performed in the last two numerical examples. The numerical verification of the optimized metamaterials was performed using commercial finite element code ABAQUS. Moreover, the underlying mechanisms of the double negative indexes in the metamaterials were originally revealed.

As for the volume constraints of the base materials in the multi-material topology optimization, there are two classic approaches: 1) a total volume constraint, and 2) individual volume-fraction constraint on each base material. The former includes all the candidate materials, which allows the optimizer to freely choose over the entire material design space. In comparison, the latter one can artificially restrict the design space while decrease the size of the feasible domain [70]. In this work, the latter approach was adopted, since a comparison study would be performed to demonstrate the effectiveness and superiority of the AAPO algorithm. It's necessary to keep the materials properties and volume constrains consistent to those used in previous work [58].

Table 2 lists the Young's modulus, PR, CTE and volume constraints of the materials used in the numerical examples. Note that in the following figures, the domains with Mat-1, Mat-2 and Mat-3 are in black, red and green colors, respectively. In Example 1, the material properties and volume constraints were consistent with those used in Ref. [58] for the purpose of comparison. In Example 2, the ratios of the Young's modulus and CTE between Mat-1 and Mat-2 were significantly different from those in Example 1. In Example 3, specific initial chiral features were pre-defined to ensure the formation of the chiral metamaterials. Other parameters were kept consistent with those in Example 2. In Example 4 and 5, the Mat-1 and Mat-2 were the same as those in Example 2, while a Mat-3 with even larger CTE was introduced in order to validate the ability to solve the tri-material topology optimization problem. For simplicity, the information of the optimized results is summarized in

Table 3
Summary of the optimized results obtained in five numerical examples.

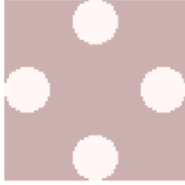

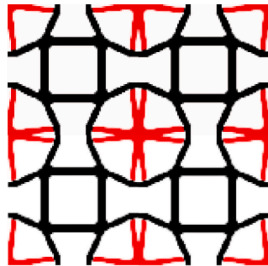
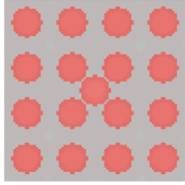
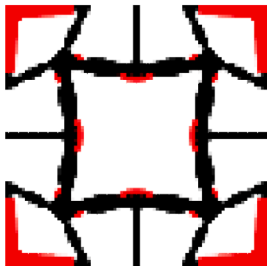
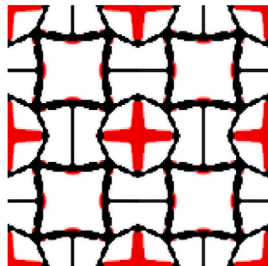


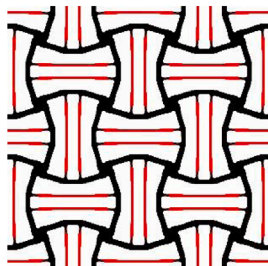
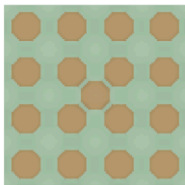

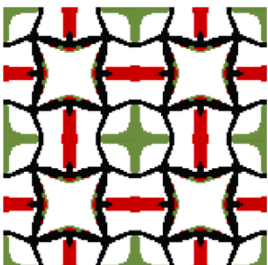

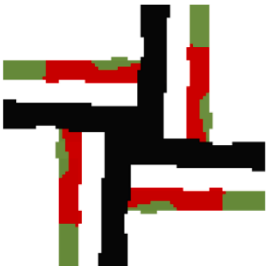
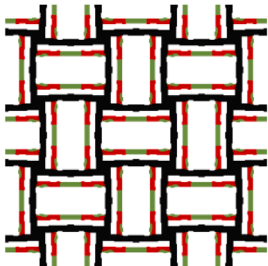
| Initial design | Unit cell | 2×2 repeated unit cells | C^H | α^H |
|---|---|---|---|---|
| <p>Example 1</p>  |  |  | $\begin{bmatrix} 0.069 & -0.038 & 0 \\ -0.038 & 0.069 & 0 \\ 0 & 0 & 0.002 \end{bmatrix}$ $v_{11}=v_{12} = -0.55$ | $\begin{bmatrix} -1.91 \\ -1.91 \\ 0 \end{bmatrix}$ |
| <p>Example 2</p>  |  |  | $\begin{bmatrix} 0.51 & -0.29 & 0 \\ -0.29 & 0.51 & 0 \\ 0 & 0 & 0.008 \end{bmatrix}$ $v_{11}=v_{12} = -0.57$ | $\begin{bmatrix} -1.58 \\ -1.58 \\ 0 \end{bmatrix}$ |
| <p>Example 3</p>  |  |  | $\begin{bmatrix} 0.055 & -0.043 & 0 \\ -0.043 & 0.055 & 0 \\ 0 & 0 & 0.001 \end{bmatrix}$ $v_{11}=v_{12} = -0.79$ | $\begin{bmatrix} -3.73 \\ -3.73 \\ 0 \end{bmatrix}$ |
| <p>Example 4</p>  |  |  | $\begin{bmatrix} 0.49 & -0.29 & 0 \\ -0.29 & 0.49 & 0 \\ 0 & 0 & 0 \end{bmatrix}$ $v_{11}=v_{12} = -0.59$ | $\begin{bmatrix} -2.32 \\ -2.32 \\ 0 \end{bmatrix}$ |
| <p>Example 5</p>  |  |  | $\begin{bmatrix} 0.42 & -0.37 & 0 \\ -0.37 & 0.42 & 0 \\ 0 & 0 & 0.003 \end{bmatrix}$ $v_{11}=v_{12} = -0.88$ | $\begin{bmatrix} -5.49 \\ -5.49 \\ 0 \end{bmatrix}$ |

Table 3, including the initial designs, topology configuration of the unit cell, periodic array and related effective properties.

3.1. Example 1: bi-material re-entrant metamaterial

3.1.1. Influences of parameter $IterInT$

Example 1. identifies an optimized design of an orthogonal

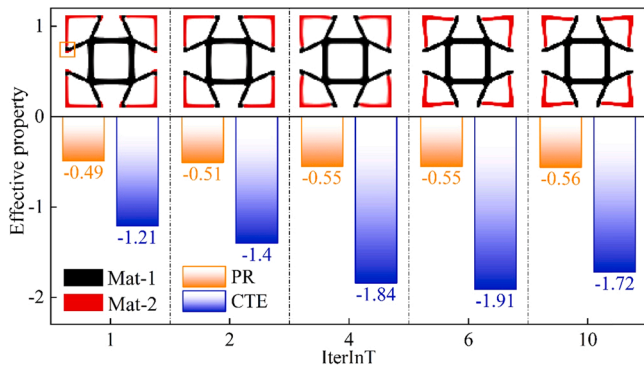


Fig. 4. Optimized results of the PR and CTE versus the parameter IterInT in the Example 1. Dispersed material distribution marked by a square is apparently reduced and eliminated eventually along with the increasing IterInT. The results identify that the proper range of IterInT should be 4–6.

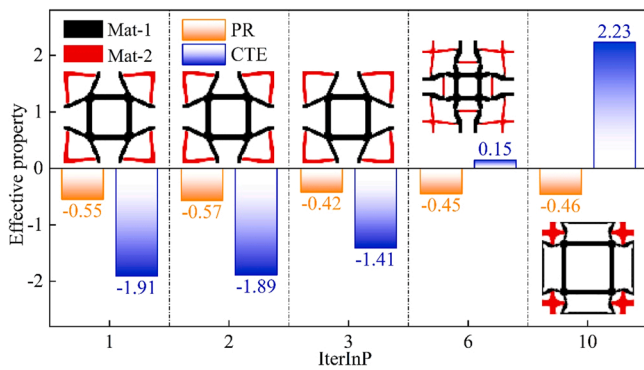


Fig. 5. Optimized results of the PR and CTE versus the parameter IterInP in the Example 1. The topological configuration and effective properties approach to be unstable along with the over increasing IterInP, and the proper range of the parameter IterInP should be 1–2.

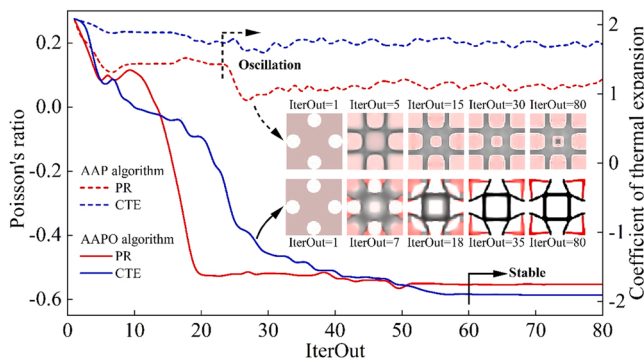


Fig. 6. Comparison between the convergence histories of the AAP and AAPO algorithm. The optimization process of the AAP algorithm shows severely oscillation, while that of the AAPO algorithm tends to be stable after 60 iterative steps.

metamaterial with extremely negative PR and negative CTE. The design domain was discretized by 80×80 quadrilateral elements. Firstly, the parameter IterInT, which controls the number of the inner loops in the sub-problem built to achieve the negative CTE, was studied. The IterInT was discussed with 5 cases, namely, IterInT= 1, 2, 4, 6, 10 with the constant IterInP = 1. Fig. 4 collects the optimized results, and the overall mechanisms are summarized as:

- i) In view of the outline of the topological configuration, the material distribution approaches to be more concentrated and stable along with the increasing IterInT. When IterInT is set as 1, as marked by a square in Fig. 4, the distributed Mat-2 (red regions) around the edges of the Mat-1 (black regions) would negatively bring in the over complicated connections, making the manufacturing to be more difficult. Fortunately, such unexpected dispersive distribution is apparently reduced and eliminated eventually as the increasing IterInT.
- ii) Both the PR and CTE are in negative values as originally expected. Their magnitudes increase rapidly along with the enlarging IterInT, and they keep stable when IterInT ≥ 4 . Besides, the over increment of IterInT up to 10 is not always beneficial, as it slightly worsens the effective properties especially for the magnitude of CTE.

Since the computational cost is proportional to the IterInT, over-low or over-high value of IterInT both have a negative influence on the optimized results. Then, Fig. 4 identifies that the appropriate range of the parameter IterInT should be 4–6.

3.1.2. Influences of parameter IterInP

Similarly, the effect of the parameter IterInP, which controlled the inner iteration number in the sub-problem built to achieve the negative PR, was studied. As clearly presented in Fig. 5, when IterInP is small, the topological configuration of the optimized results is similar with each other, while the magnitudes of the PR and CTE are different. The topological configuration and effective properties vary rapidly as IterInP is enlarged. The above results mainly stem a fact that the parameter l in Eq. (9) is highly related to the outer iteration number. During the optimization progress, the first term $\lambda^l(C_{1111} + C_{2222})$ gradually vanishes, while the second term C_{1122} gets minimized, i.e. the Poisson's ratio is minimized. Generally, the parameter l is equal to the value of the outer loops. When the parameter IterInP is relatively high, the parameter l would be approximately kept as a constant, making the first term $\lambda^l(C_{1111} + C_{2222})$ of the leading domination. These would bring in negative affect on the term C_{1122} , generating the design with worsen PR.

The over large IterInP has remarkably negative effects on the optimized results, especially on the CTE. The CTE is even positive when the topological configuration approaches to be unstable, completely deviated from the original target. Obviously, the careful selection of IterInP could improve the computational performance and outcome of the AAP algorithm. Hence, as far as finding the stable topological configurations and effective properties, the parameter IterInP should be 1–2.

3.1.3. Convergence of the switch strategy

Based on the above analysis, the optimized result under IterInT= 6 and IterInP= 1 is listed in Table 3. The final design has clear boundaries and concentrated material distribution. The convergence histories of the effective properties and topological evolution are shown in Fig. 6. At the initial iterative steps, the aggregation of different materials occurs, leading to the dramatic variations in the effective properties. The main re-entrant feature and bi-material layout are formed within the first 30 steps. Afterwards, the material distribution changes only slightly in the local locations. After near 60 iterative steps, the optimization is stable and quickly approaches to the pre-defined convergent condition where the optimization is terminated within 80 iterations.

For comparison, the weighted sums method was settled as the objective function in each inner loop according to the following formulation:

$$f_{obj} = w_1fp + w_2ft \tag{11}$$

where w_1 and w_2 are the weighting factors of which the value was 0.5. The convergence history is shown in the upper part of Fig. 6. The aggregation of different materials only occurs at the initial steps and the topological configuration of the final design are blurry. The oscillation of the effective properties is obvious, indicating that the optimization

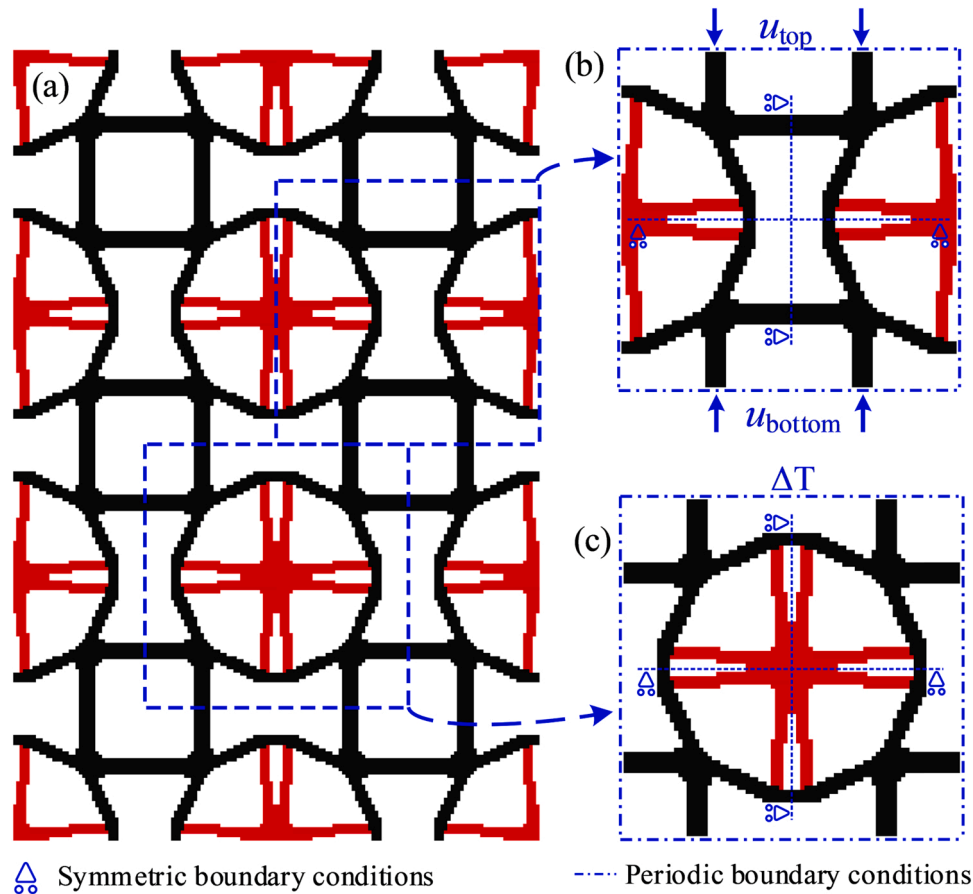


Fig. 7. Numerical model with boundary conditions for Example 1. (a) 3×2 repeated unit cells. The representative unit cells extracted to respectively illustrate the deformation mechanisms of (b) auxetic effect and (c) negative thermal expansion effect.

process is hard to convergence stably. Worst of all, both the PR and CTE of the final design are of positive value, which is far from the design objective. These results firmly verify the effectiveness of AAPO algorithm from the opposite side.

3.1.4. Deformation mechanism

In order to clearly reveal the deformation mechanisms of the negative indexes in the optimized metamaterials, the finite element analysis (FEA) was performed. For verifying the negative PR, the boundary conditions illustrated in Fig. 7(b) were applied on a representative cell. The displacements along the vertical direction were compressed at the top and bottom sides, and the symmetrical boundary conditions and periodic boundary conditions (PBCs) were considered. According to the contours on the deformed shape given in Table 4, the induced horizontal strains are -1.41% and -2.82% under the loading strains of $\epsilon_y = -2.5\%$ and -5% , respectively. The numerically calculated PR is -0.56 , which is quite close to the topology optimized results. Furthermore, a representative unit cell is extracted to illustrate the deformation mechanism in Table 4. Obviously, the ribs with Mat-1 (black) form a remarkable re-entrant geometry. When these ribs suffer the vertical compression, the re-entrant geometry enables the ribs with Mat-2 (red) to deform towards the inside direction as marked by the arrows, leading to the auxetic effect, namely, negative Poisson's ratio.

As for the numerical simulation for the negative CTE, the boundary conditions and loading temperature are illustrated in Fig. 7(c). In addition to the geometry feature, the material layout is another major consideration in the analysis. Therefore, different from Fig. 7(b), another representative unit cell is exclusively extracted to include the bi-material feature in Fig. 7(c). The thermal strains ϵ_T under the temperature variations $\Delta T = 0.005^\circ\text{C}$ and 0.01°C are of -0.98% and -1.95% ,

respectively. The numerically calculated CTE is -1.95 . As shown in Table 4, in the representative cell, four ribs with Mat-2 (red, large CTE) are intersected as a cross and are surrounded by an annulus which is consisted of the ribs with Mat-1 (black, low CTE). The large thermal expansion of the inner cross drives its connected ribs to deform towards the outside direction. Accordingly, the junctions A, B, C and D move towards the inside direction as marked by the arrows, resulting in the shrinkage along both horizontal and vertical directions, verifying the negative thermal expansion.

The obtained metamaterial in this numerical example can be classified as a kind of porous metamaterial with re-entrant geometry feature and bi-material layout. In the direct design, these features have been demonstrated to be essential for obtaining the double negative indexes [16]. Besides, the FEA calculated values of the PR and CTE are very close to the results in Table 3. That is the negative PR and CTE are successfully integrated into one metamaterial through the proposed algorithm.

3.2. Example 2: bi-material re-entrant metamaterial

3.2.1. Influences of parameter $IterInT$

In this example, the related parameters are consistent with those in the Example 1 except the different material properties as listed in Table 2. As shown in Fig. 8, the results of the parameter $IterInT$ are summarized as:

- i) As the $IterInT$ increases, the material distribution approaches to be more concentrated and stable. When $IterInT$ increases from 1 to 4, the tiny branches are obviously suppressed. When $IterInT$ increases from 6 to 10, the distributed Mat-2 (red regions) around the Mat-1 (black regions) are reduced and finally are eliminated.

Table 4

Numerical simulation and mechanism illustration of Example 1. Overlay before and after deformation in the contours illustrates the auxetic and negative thermal expansion.

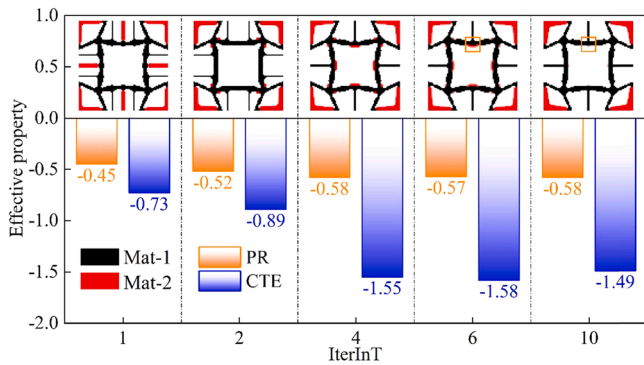
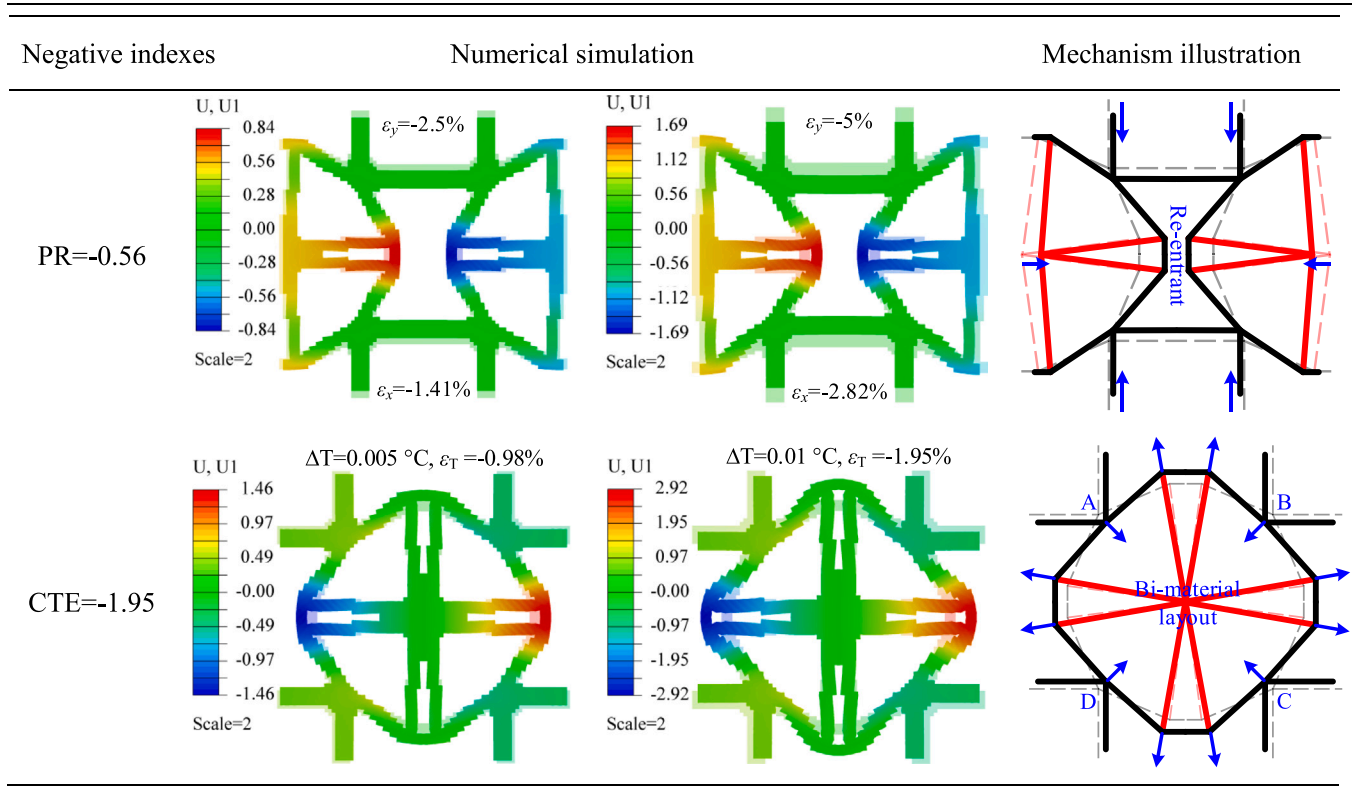


Fig. 8. Optimized results of the PR and CTE versus the parameter IterInT in Example 2. The increasing of IterInT reduces the dispersed material distribution marked by a square. These results suggest the proper range of IterInT should be 4–6. (For interpretation of the references to colour in this figure, the reader is referred to the web version of this article.)

ii) The effective properties are stable when $IterInT > 4$, while the over-high value of IterInT has a slightly negative influence on the optimized result.

Hence, as far as finding the stable designs with minimum computational cost, the proper range of the parameter IterInT should be 4–6.

3.2.2. Influences of parameter IterInP

The influences of the parameter IterInP is analyzed under the constant IterInT = 6. As shown in Fig. 9, the enlargement of IterInP initially has a positive influence on improving the magnitude of the negative PR, while it oppositely worsens the CTE. The topological configuration oscillates and approaches to be unstable, as IterInP is continuously

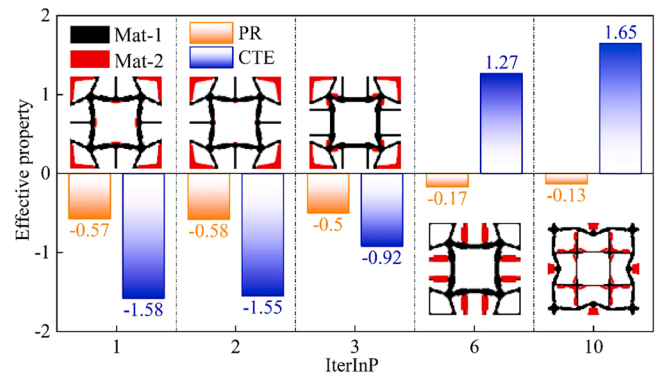


Fig. 9. Optimized results of the PR and CTE versus the parameter IterInP in Example 2. The enlargement of IterInP has a negative influence on the optimized results, and the proper range of the parameter IterInP should be 1–2.

enlarged. Similarly, the magnitudes of the PR and CTE are reduced quickly. The CTE is even positive when the parameter is increased to be 6. Accordingly, IterInP should be 1–2.

3.2.3. Deformation mechanisms

The results of the optimized design under IterInT= 6 and IterInP= 1 are listed in Table 3, and the convergence histories are given in Fig. 10. A star-like re-entrant geometry, which is responsible for the generation of the negative PR, is gradually formed at the initial steps. Driving by the negative CTE demand, the Mat-2 (red regions) aggregates at the four corners of the design domain. As the iterative number increasing, the meaningless features like the islands at the center are eliminated, and the objective function values reduce gradually. The main configuration is formed within the first 50 steps and keeps stable with only a few

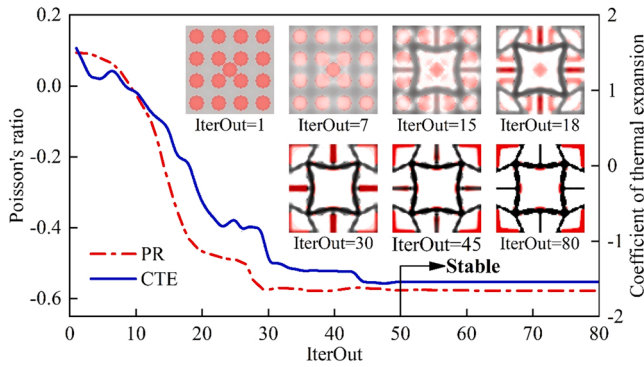


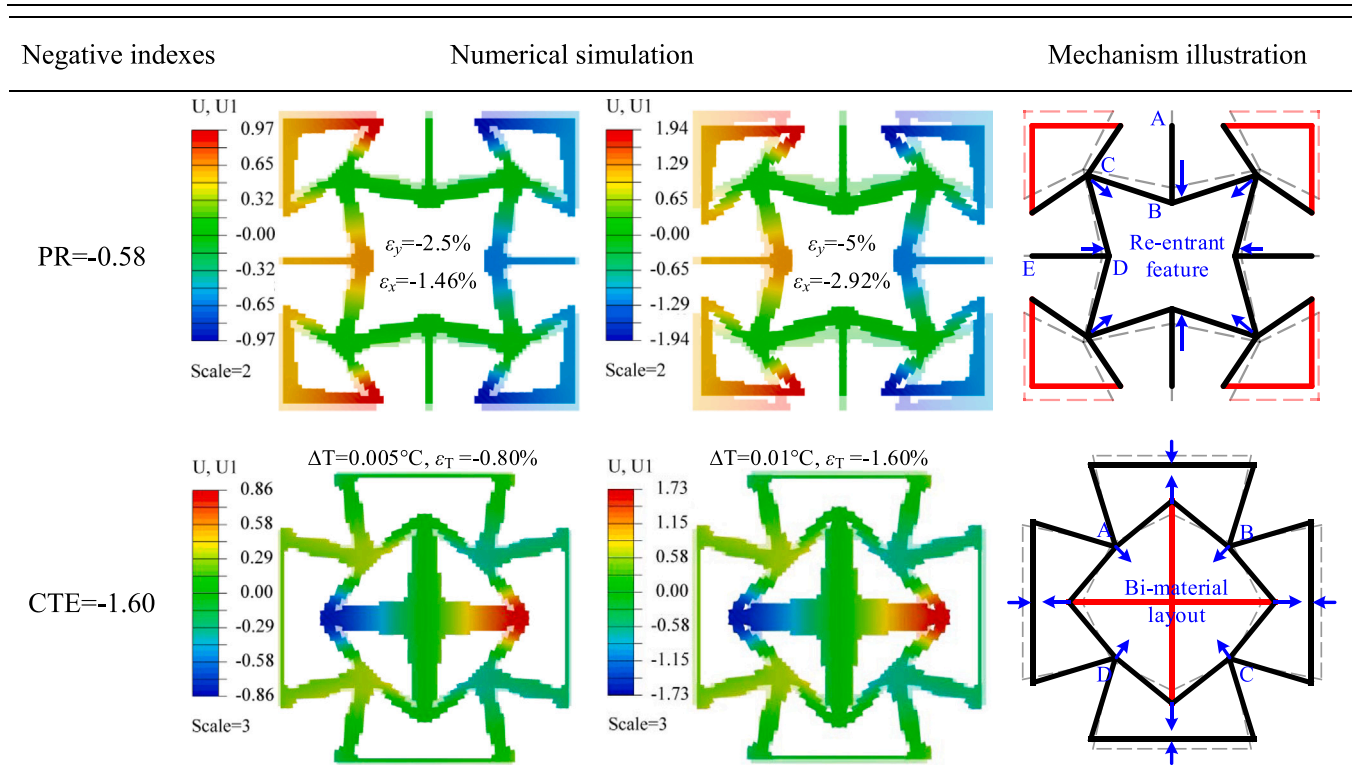
Fig. 10. Convergence histories of the Poisson's ratio and coefficient of thermal expansion in Example 2. The optimization process is stable after 50 steps.

changes on the boundaries until the optimization process converges.

As given in Table 5, using the same loading and boundary conditions adopted in Example 1, the contour evolutions under both mechanical and thermal loadings clearly demonstrate the negative Poisson's ratio and thermal expansion of which the values are -0.58 and -1.60 , respectively. For the unit cell extracted to illustrate the auxetic effect, the major feature is a star-like shaped re-entrant geometry. Considering the symmetry, when the rib AB is compressed, the re-entrant geometry allows the junction C to move towards inside. Then, the horizontal rib DE is forced to deform towards the center, generating the auxetic effect. Similarly, a different representative unit cell, which exactly includes the bi-material layout, is used to analyze the thermal expansion. The two ribs with Mat-2 (red, large CTE) are intersected at a cross, which is surrounded by the outside ribs with Mat-1 (black, low CTE). The large thermal expansion of the inner cross, induced by the temperature variation, drives the movement of the connected ribs towards outside.

Table 5

Numerical simulation and mechanism illustration of Example 2. Overlay before and after deformation in the contours illustrates the auxetic and negative thermal expansion.



Correspondingly, the junctions A, B, C and D move towards the center (indicated by the arrows). Then, the profile of the unit cell induces the resulted shrinkage, namely, the negative thermal expansion.

Actually, many similar star-shaped metamaterials have been designed by the direct design strategy [9,71] which can only give one function of the negative PR. According to the analysis of the deformation mechanism, introducing and redistributing different base materials to specifically generate the bi-material layout additionally integrates one more function of negative CTE into the metamaterial, making it to be multi-functional. Similar to the previous examples, the results herein confirm the convergence and stability of the developed algorithm.

3.3. Example 3: bi-material chiral metamaterial

3.3.1. Influences of parameter IterInT

Here, the bi-material chiral metamaterial was originally developed by topology optimization. The related design parameters were consistent with those in the Example 2, while only a specific initial chiral feature was pre-defined to ensure the chiral deformation mechanism in the final design [50].

As clearly presented in Fig. 11, the tiny branches are obviously suppressed, as IterInT increases from 1 to 4. Afterwards, when IterInT increases from 4 to 10, Mat-2 (red regions), which distributes around the Mat-1 (black regions), is effectively reduced. That is increasing IterInT enables the material distribution approach to be concentrated and stable. The magnitudes of the negative PR and CTE are stable, when $IterInT > 4$. However, the over increment of IterInT up to 10 is not beneficial to further enlarge the magnitudes, since the dispersive materials are all eliminated. Accordingly, the proper range of the parameter IterInT should be 4–6.

3.3.2. Influences of parameter IterInP

Similarly, the influences of the parameter IterInP were studied under

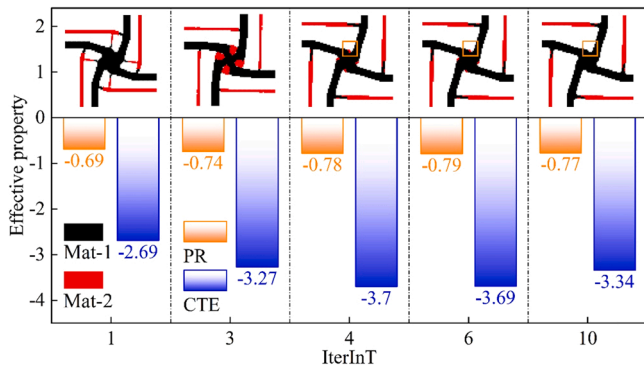


Fig. 11. Optimized results of the PR and CTE versus the parameter IterInT in the Example 3. The dispersed material distribution marked with a square are apparently reduced along with increasing IterInT, and the appropriate range of IterInT should be 4–6.

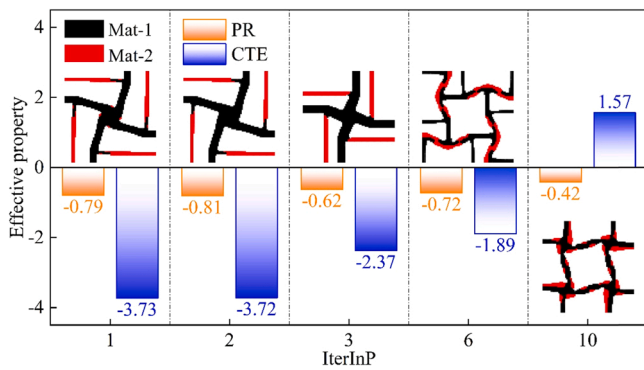


Fig. 12. Optimized results of the PR and CTE versus the parameter IterInP in Example 3. The proper range of IterInP should be 1–2.

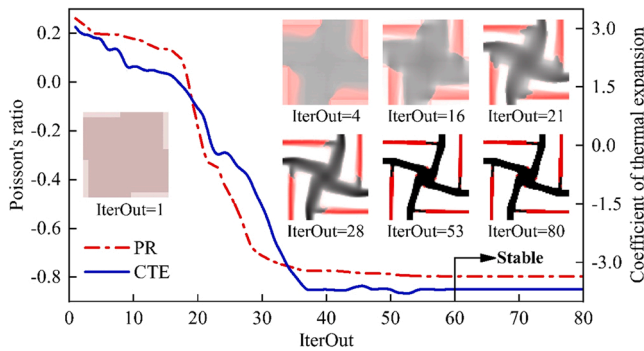


Fig. 13. Convergence histories of the Poisson's ratio and coefficient of thermal expansion in Example 3. The optimization progress becomes stable after 60 steps.

the constant IterInT = 6. As shown in Fig. 12, the parameter IterInP has the remarkable influences on the topological configurations and the magnitudes of the PR and CTE. The enlargement of IterInP initially has slightly positive influence on improving the magnitude of the negative PR, while oppositely worsens the negative CTE. However, the optimized results vary dramatically and approach to be unstable, as IterInP is continuously enlarged. The CTE even shifts to be positive, completely deviated from the original objective. Accordingly, the range of the IterInP should be 1–2.

3.3.3. Deformation mechanism

The results of the optimized design under IterInT = 6 and IterInP = 1

are listed in Table 3. As shown in Fig. 13, the effective properties vary dramatically in the first few iterations along with the pronounced change in the topological configuration. The Mat-2 (red regions) aggregate and form four slender ribs to achieve the negative CTE. The boundaries and material distribution evaluate to be clear and concentrate along with the optimization progress. After 60 steps, the optimization is stable and quickly approaches to convergence.

As given in Table 6, the simulated negative indexes of the PR and CTE are -0.86 and -3.94 , respectively. To illustrate the negative indexes, a representative unit cell, in which the major architecture is composed of four circular nodes and the connecting ribs, is extracted. When the ribs suffer the vertical compression, the bending-dominated deformation of the connecting ribs drives every unit (marked by a blue frame) rotates in the opposite directions related to its immediate neighbor. Then, the negative Poisson's ratio is induced. Besides, the bi-material layout is formed as the ribs with Mat-2 (red, large CTE) are surrounded by the ribs with Mat-1 (black, low CTE). The large thermal expansions of the ribs, e.g. AB and CD, drive the connected ribs rotate around the circular nodes. Then, the profile of the unit cell presents the shrinkage, namely, the negative thermal expansion.

It should be noted that up to now, all the chiral multi-functional metamaterials [19,32–34] were designed through the direct design strategy, which means only scattered designs have been proposed. Chiral multi-functional metamaterials, which is developed exactly by topology optimization is first presented by this work, filling the vacancies in metamaterial topology optimization. Furthermore, it's obvious that the magnitudes of both PR and CTE in the chiral metamaterial are much higher than those in the re-entrant one, suggesting that the chiral one has more excellent multi-functional potential.

3.3.4. Universality of the controlling parameters

According to the above analysis, the influence of the controlling parameters IterInT and IterInP on the optimization process are discussed not only in a qualitative way, but also in a quantitative test with the definitive values. In detail, as shown in Figs. 4, 8 and 11, the increasing IterInT will promote the aggregation of materials and bring in concentrated topological configurations. However, the over increment of IterInT is not always beneficial, as it slightly worsens the magnitude of the negative indexes. Considering the computational cost, the IterInT should be 4–6 to achieve a balance between effectiveness and efficiency. Besides, the overlarge IterInP also has the remarkably negative effects on the optimized results as suggested by the results in Figs. 5, 9 and 12. The topological configurations tend to be unstable, and the CTE is even positive, completely deviated from the original target, suggesting that IterInP should be 1–2.

It is clear that the controlling parameters in the AAPO algorithm are problem-independent, since the same proper ranges are demonstrated to be quite applicable in all numerical examples. This identified universality increases the generality and utility of the developed algorithm. Furthermore, the optimization progresses shown in Figs. 6, 10 and 13 become stable after 50–60 steps, suggesting that the developed algorithm possesses superior convergence.

3.4. Example 4: tri-material re-entrant metamaterial

In this example, the design space was enlarged from bi-material to tri-material (both not containing void phase), which has not been proposed yet. The Mat-1 and Mat-2 were identical with those in Example 2 while a new material Mat-3 was additionally introduced. The controlling parameters IterInT and IterInP were set as 6 and 1, respectively. The information of the obtained metamaterial is listed in Table 3. Although the geometry of the unit cell is similar with that in Example 2, the material distribution is obviously different. Moreover, the magnitude of the negative CTE is much higher, since a third material with large CTE is introduced in this example (see Table 2).

The simulated negative indexes of the PR and CTE are -0.61 and

Table 6

Numerical simulation and mechanism illustration of Example 3. Overlay before and after deformation in the contours illustrates the auxetic and negative thermal expansion.

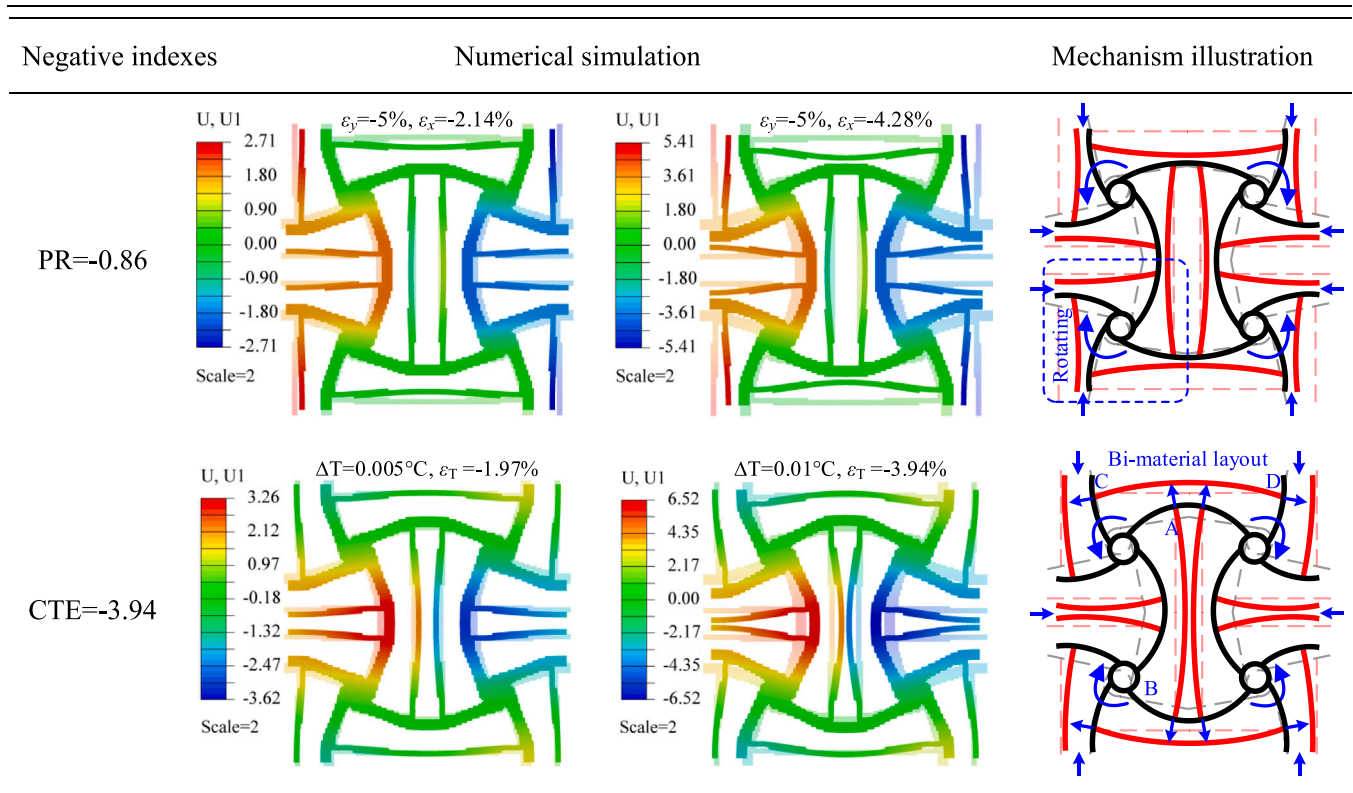


Table 7

Numerical simulation and mechanism illustration of Example 4. Overlay before and after deformation in the contours illustrates the auxetic and negative thermal expansion.

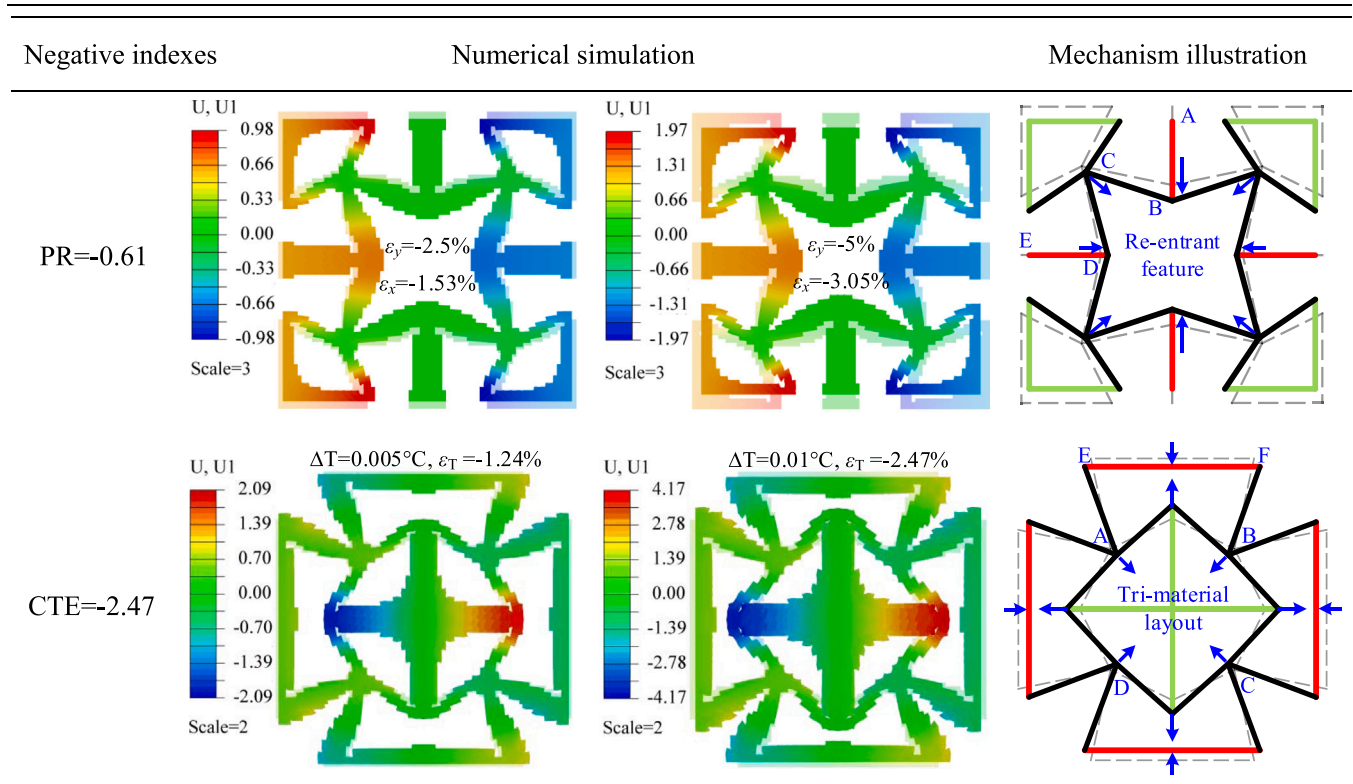
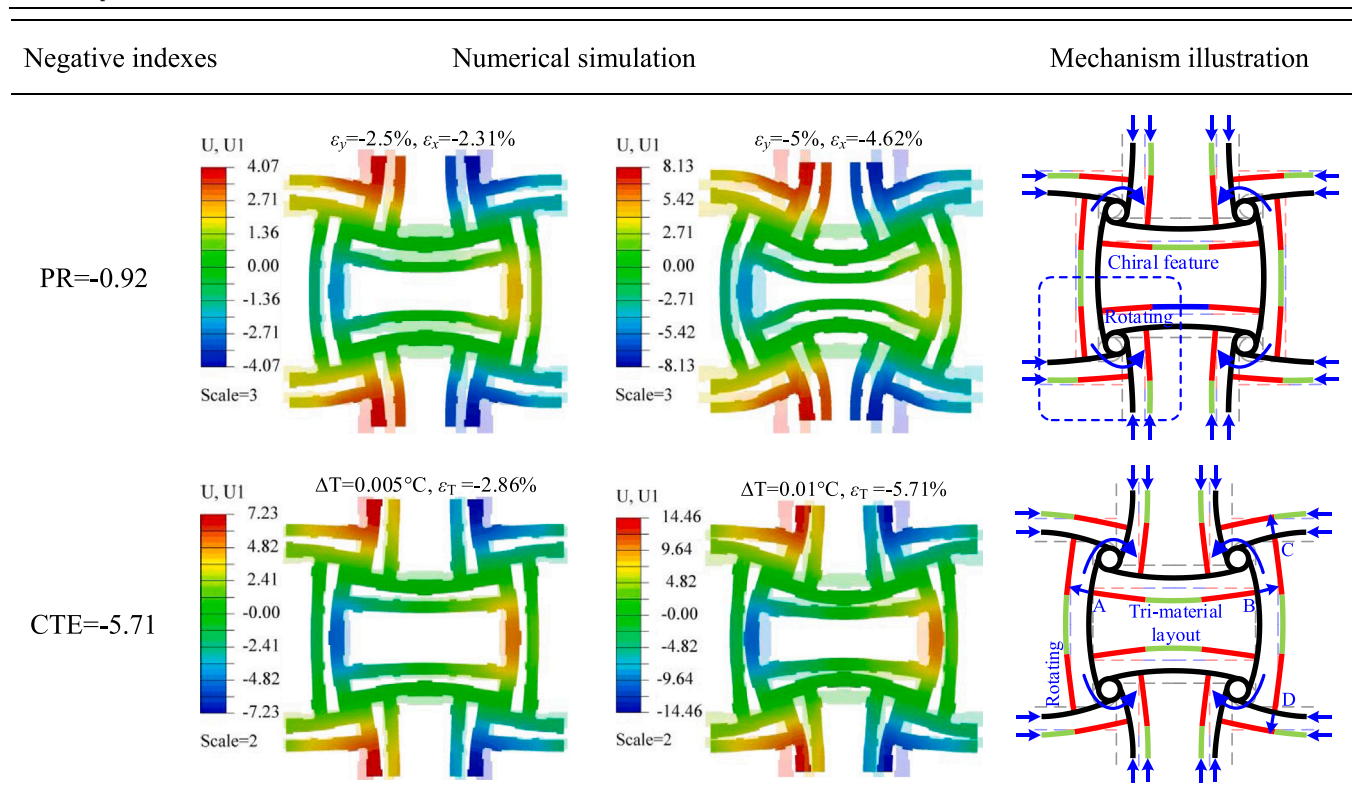


Table 8

Numerical simulation and illustrated deformation mechanisms for Example 5. Overlay before and after deformation in the contours illustrates the auxetic and negative thermal expansion.



– 2.47, respectively. The extracted star-like shaped re-entrant feature in the unit cell is strongly similar to that obtained in Example 2. Then, the deformation mechanism (see Table 7) of the negative PR here is identical to that in the Example 2 (see Table 5). Moreover, a representative unit cell, which exactly contains the tri-material layout, is also illustrated in Table 7. Actually, there are three different sets of ribs. The ribs with Mat-3 (blue, large CTE) form an inner cross in the center, while the ribs with Mat-2 (red, moderate CTE) locate at the outside of the four edges. The rest ribs with Mat-1 (black, low CTE) act as the connections between the inner cross and outside edges. When suffering a temperature increment, the large thermal expansions, generated by the inner cross, eventually induce the movement of the junctions A, B, C and D towards the center, leading to the obvious shrinkage along both the horizontal and vertical directions. That is the negative thermal expansion is generated. Moreover, it should be noted that the relative large thermal expansions of the outside ribs with Mat-2 also enhance the movement of the junctions A, B, C and D towards the center, revealing the reason why the negative CTE magnitude in this metamaterial is larger than those in the Example 1 and 2. Indeed, the variety in base materials has a negligible influence on the deformation pattern, only improves the magnitudes of the effective properties.

3.5. Example 5: Tri-material chiral metamaterial

This example presents the results of the tri-material chiral metamaterial, which is still not reported in literature. The related parameters were consistent with those in the Example 4, except that the specific initial chiral feature was pre-defined (see Table 3). The magnitudes of both negative PR and CTE are higher than those of the re-entrant tri-material metamaterial in Example 4, indicating that the chiral type has relatively more excellent multi-functional potential. Accordingly, the capability of the AAPO method to seek for tri-material multi-functional metamaterials is well identified.

The simulated negative indexes of the PR and CTE are – 0.92 and – 5.71, respectively, as collected in Table 8. A representative unit cell is extracted in which the major architecture is composed of the circular nodes connected by the ribs. When the ribs suffer the compression along the vertical direction, driven by the bending-dominated deformation of the connecting ribs, every circular node rotates in the opposite direction related to its neighbor. Accordingly, the negative Poisson's ratio is induced. Furthermore, for the thermal expansion, the ribs with large CTEs (Mat-2, red; Mat-3, blue) are surrounded by the outside ribs with low CTE (Mat-1, black). The large thermal expansions of the ribs, e.g., AB and CD, induced by the temperature variation, drive the connected ribs rotate around the connected circular nodes, generating the negative thermal expansion. Besides, the contour evolutions in Table 8 under both mechanical and temperature loads also clearly demonstrate the negative Poisson's ratio and thermal expansion.

3.6. Comparison and discussion

As mentioned in Introduction, many the metamaterials have either only negative Poisson's ratio or sole negative thermal expansion. In contrast, only a few numbers of metamaterials, as fully summarized in Fig. 14, incorporate the double negative indexes of PR and CTE. From the view of the material variety, these metamaterials can be classified as the bi-material and tri-material types. Besides, the geometrical feature identifies them as the re-entrant and chiral types. In the view of the design strategy, most of the metamaterials were obtained through the direct design (in the outside annulus of Fig. 14), while only a few of ones were designed by topology optimization.

Overall, Fig. 14 indicates that the direct design strategy always generates scattered results, as can be seen that every kind of the metamaterial is given by different individual work (marked by their reference number). This scattered feature originates from the nature of experience- or inspiration-based design process as given in Fig. 1(a). In

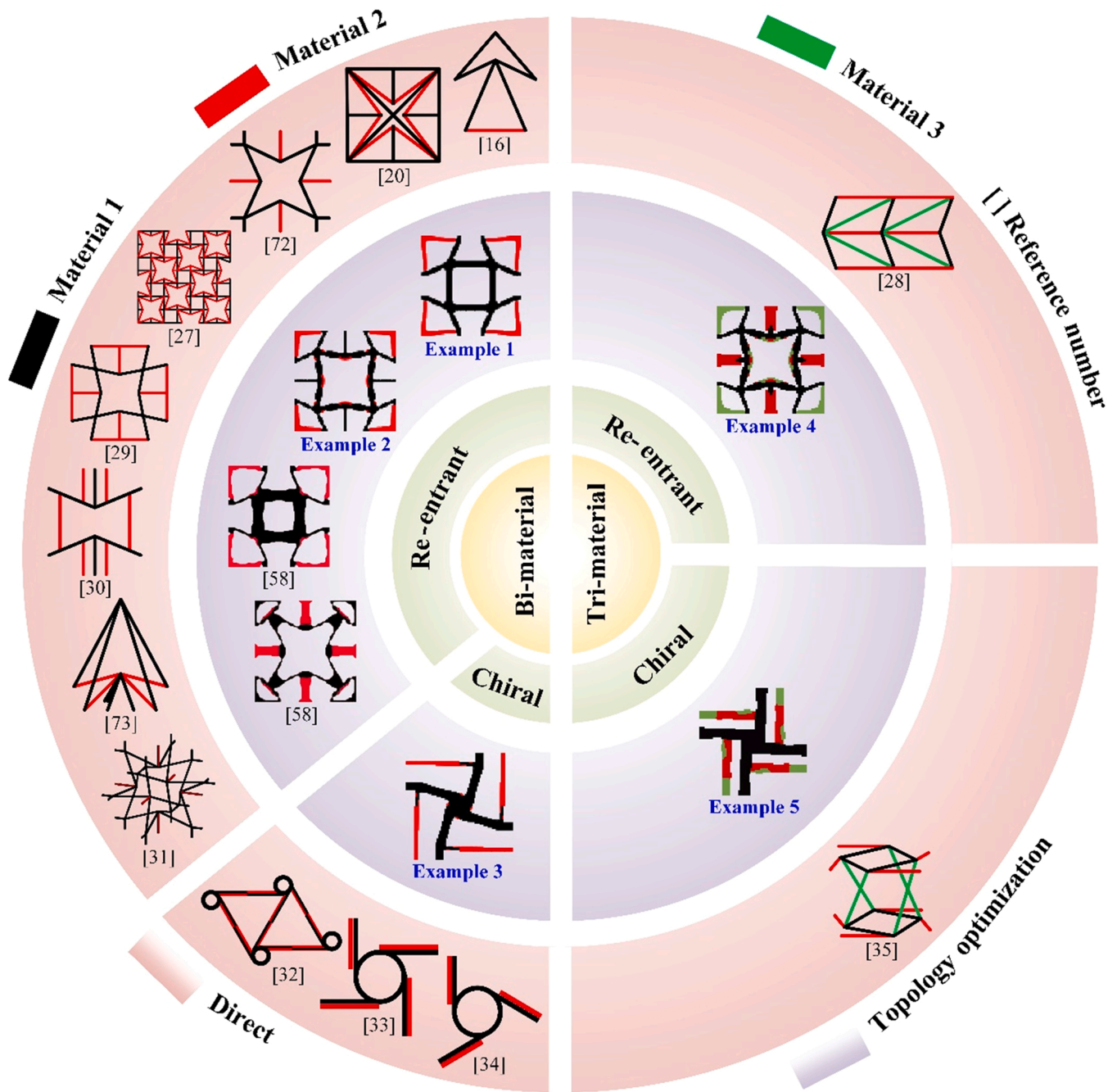


Fig. 14. Comparison of the metamaterials incorporating the double negative indexes of PR and CTE proposed in literature and in current work. Scatted metamaterials were obtained through the direct design strategy, while the AAPO topology optimization algorithm uniformly generated a series of metamaterials including the bi-material and tri-material, re-entrant and chiral types (marked by Example 1–5).

contrast, a series of metamaterials (Example 1–5 marked in Fig. 14), which cover the bi-material and tri-material, re-entrant and chiral types, are uniformly obtained by a originally developed AAPO topology optimization algorithm. These systematical design ability and advantage are originated and ensured by the nature of the mathematical programming-based topology optimization as illustrated in Fig. 1(b).

As for the metamaterials obtained here, most of them have the own special configurations and deformation mechanisms. The material properties and volume constraints employed in Example 1 were identical with those in Ref. [58], leading to the similarity in the metamaterial configurations. However, the CTE of the metamaterial in Example 1 is much higher than that given in Ref. [58]. This comparison indicates that the AAPO algorithm is of effectiveness to obtain superior performance.

In addition, the metamaterial obtained in Example 2 contains a star-shaped configuration (see Fig. 14), which is found in metamaterials with negative Poisson’s ratio. However, the topologically optimized bi-material layout obviously differs from the material distribution in existing literatures [58,72,73], exclusively bringing out new deformation mechanism (Example 2).

The metamaterials obtained in Example 3 is a bi-material chiral type, which has never been designed by topology optimization as shown in Fig. 14. The feature of the chiral metamaterials given by the direct design [32–34] is that the ribs are consisted of the bi-material strips which usually induce the bending deformation and rise the manufacturing complexity. Differently, the slender ribs in the metamaterials herein are consisted of the single material, which brings a

Table 9

The properties of the base materials PVA and nylon.

| Material | Young's modulus | Poisson's ratio | Coefficient of thermal expansion |
|----------|-----------------|-----------------|----------------------------------|
| PVA | 4765.0 (MPa) | 0.370 | 21.0 (ppm/°C) |
| Nylon | 1330.0 (MPa) | 0.394 | 166.0 (ppm/°C) |

Table 10

Process parameters used in the additive manufacturing for the mechanical testing specimens.

| Parameters | Values | Parameters | Values |
|---------------------------|--------|------------------------|--------|
| Printing temperature (°C) | 230.0 | Raster width (mm) | 0.23 |
| Printing speed (mm/s) | 20.0 | Filling percentage (%) | 100.0 |
| Nozzle diameter (mm) | 0.25 | Filling patterns | Line |
| Layer thickness (mm) | 0.06 | | |

novel topological configuration. From the perspective of engineering applications, this new topological configuration could significantly reduce the complicated and unnecessary connections, simplifying the practical manufacture process.

Moreover, the metamaterials obtained in Examples 4 and 5 are tri-material types, in which their properties are better than the bi-material ones, especially the negative thermal expansion. It should be noted that these tri-material metamaterials have not been devised by topology optimization as summarized in Fig. 14, and only two cases were presented by direct design strategy. The material variety could effectively improve the magnitudes of the effective properties, while has a negligible influence on the deformation pattern. Besides, the magnitudes of the PR and CTE in the chiral type metamaterials are much higher than those in the re-entrant ones regardless bi-material or tri-material, suggesting that the chiral type has more excellent multi-functional potential. These results could firmly suggest the effectiveness of the AAPO algorithm and provide a general guidance to the direct design of multi-functional metamaterials.

4. Additive manufacturing and experiments

4.1. Multi-material additive manufacturing

The main purpose of this section is to experimentally validate the effectiveness of the proposed algorithm and corresponding metamaterials. Taking advantage of the multi-material additive manufacturing, the topology-optimized metamaterials were successfully fabricated here. The Poisson's ratio and thermal expansion experiments were performed to measure the negative indexes of the PR and CTE. The additive manufacturing process requires no extra process and could be an effective way to fabricate metamaterials consisted of multiple base

materials. As a representative, in our previous work [74], two polymers, polyvinyl alcohol (PVA) and nylon, were incorporated in the metamaterials through additive manufacturing. Accordingly, these two polymers were used as the base materials. Their properties are listed in Table 9.

The CTEs were obtained in Ref. [74] of which the averaged values are $\bar{\alpha}_{PVA} = 21\text{ppm}/^\circ\text{C}$ and $\bar{\alpha}_{Nylon} = 166\text{ppm}/^\circ\text{C}$. The Young's modulus and Poisson's ratio were measured following the ASTM Standards D638–14 in this work. The basic additive manufacturing parameters are listed in Table 10.

The tensile experiments were conducted by stretching the specimens with a constant loading speed of 0.05 mm/s using a universal testing machine, MTS E45.105-B. Fig. 15(a) shows the stress-strain responses of three repeated tests of the base materials. Accordingly, the averaged Young's modulus $\bar{E}_{PVA} = 4765\text{MPa}$ and $\bar{E}_{Nylon} = 1330\text{MPa}$ were obtained according to the slopes. Meanwhile, the averaged Poisson's ratios $\bar{\nu}_{PVA} = 0.376$ and $\bar{\nu}_{Nylon} = 0.389$ were measured through the Digital Image Correlation (DIC) method [75]. The longitudinal and transverse strains were measured through the captured images of the specimens with random speckles as shown in Fig. 15(b).

With the obtained the properties of the base materials, the re-entrant and chiral metamaterials with negative PR and CTE were designed using the developed AAPO algorithm. The volume constraints of the PVA and nylon were 0.26 and 0.13, respectively. The topological configurations and properties are listed in Table 11. Note that the PVA and nylon are in light and dark color, respectively. Afterwards, these metamaterials were additively manufactured by the same 3D printer with the same process parameters listed in Table 10. These metamaterials were used for the Poisson's ratio and thermal expansion experiments in Sections 4.2 and 4.3.

4.2. Poisson's ratio experiments

In the Poisson's ratio experiments, the additively manufactured specimens (3×3 unit cells, Fig. 16(a)) were pulled by applying a static tensile displacement from deformation to rupture with a specific interval of 0.5 mm. The tests were repeated on two independent specimens. By using ImageJ software, the longitudinal and transverse strains were calculated by tracking the reference points as illustrated in Fig. 16(c):

$$\varepsilon_x = \frac{1}{N} \left(\frac{\Delta|L_1^x|}{|L_1^x|} + \frac{\Delta|L_2^x|}{|L_2^x|} + \dots + \frac{\Delta|L_n^x|}{|L_n^x|} \right) \quad (12)$$

$$\varepsilon_y = \frac{1}{N} \left(\frac{\Delta|L_1^y|}{|L_1^y|} + \frac{\Delta|L_2^y|}{|L_2^y|} + \dots + \frac{\Delta|L_n^y|}{|L_n^y|} \right) \quad (13)$$

where $|L_1^x|$ represents the original horizontal length between the refer-

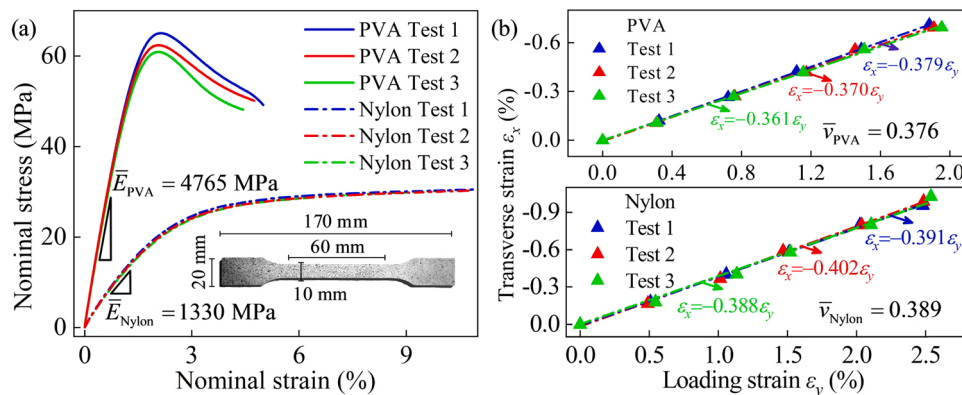






Fig. 15. (a) stress versus strain and (b) transverse strain versus loading strain under tensile experiments. The Young's modulus ($\bar{E}_{PVA} = 4765\text{MPa}$, $\bar{E}_{Nylon} = 1330\text{MPa}$), Poisson's ratio ($\bar{\nu}_{PVA} = 0.376$, $\bar{\nu}_{Nylon} = 0.389$) were obtained. (The tensile specimen with the material PVA is inserted in (a) for representative.)

Table 11
Overview of the re-entrant and chiral metamaterials obtained through the AAPO algorithm. The unit of the CTE is ppm/°C.

| Types | Unit Cell | 2×2 arrays | Properties |
|------------|--|---|-------------------------|
| Re-entrant |  |  | PR=-0.64 CTE=-42.04 |
| Chiral |  |  | PR=-0.97 CTE=-483.27 |

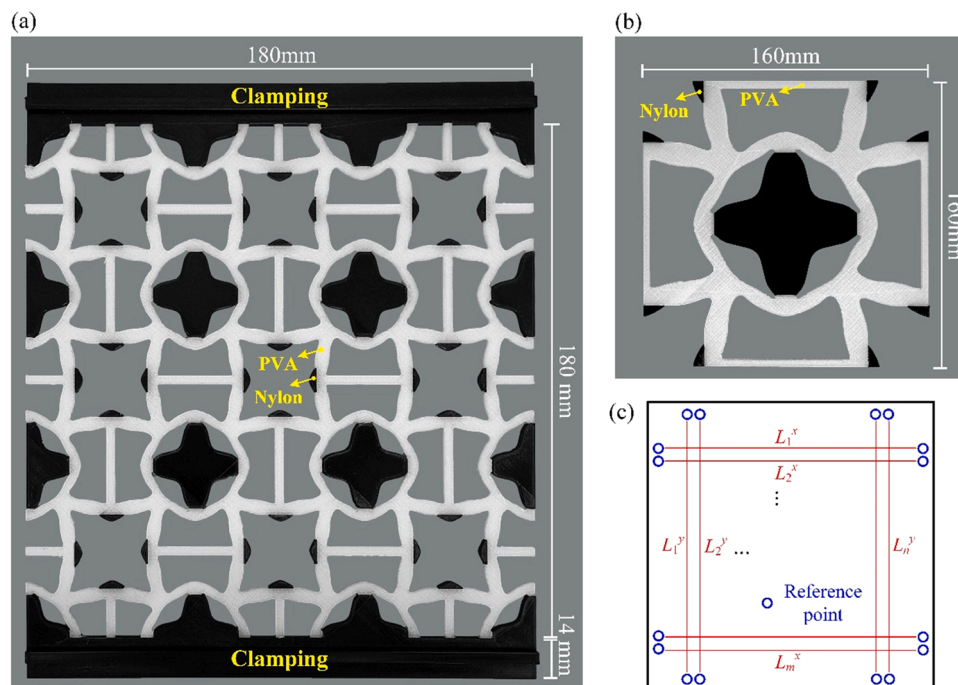


Fig. 16. As a representative, the specimens of the re-entrant type metamaterial manufactured for the (a) Poisson's ratio and (b) thermal expansion experiments. (c) Illustration to calculate the strains in horizontal and vertical directions. (Colors: Nylon, PVA and the background are in black, white and grey, respectively.).

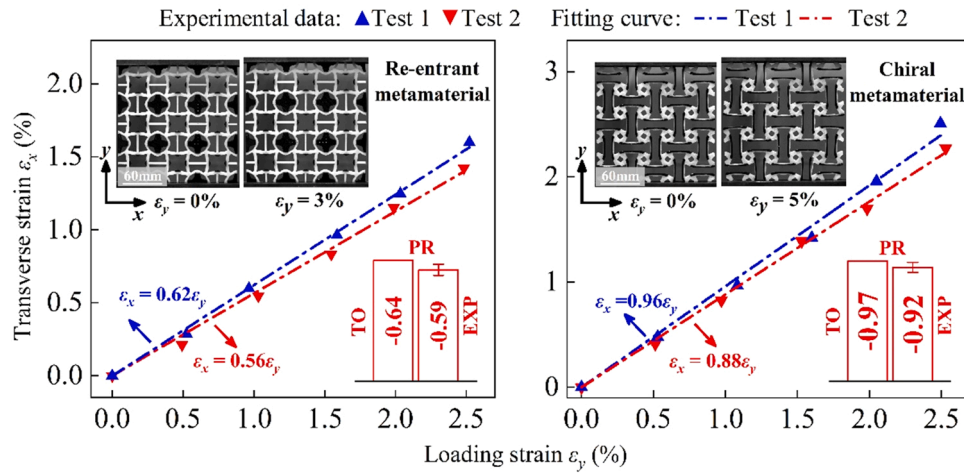


Fig. 17. The results of the Poisson's ratio experiment including the experimental data, fitted curves and the digital images of the deformation process of the topology-optimized metamaterials. (The digital images of the specimen under different tensile strain are included for illustration.)

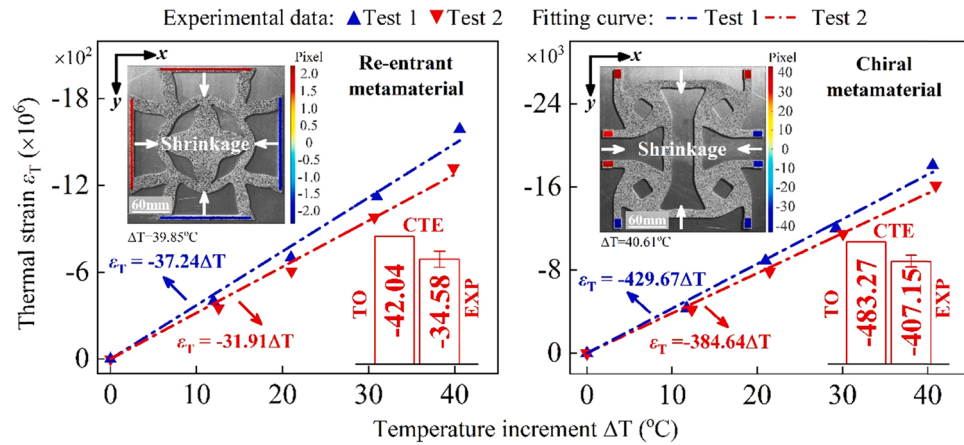


Fig. 18. The results of the thermal expansion experiment including the experimental data, fitted curves, digital images and related thermal strain contours of the deformation process of the topology-optimized metamaterials. (The digital images of the deformed specimen with an overlay of the thermal displacement contour are included for illustration.)

ence points. $\Delta|L_i^x|$ represents corresponding deformation. N represents the total number of the reference points.

The deformation images and experimental data are collected in Fig. 17. The extensions along the horizontal direction under the vertical stretching suggest the expected auxetic effect, namely, the negative Poisson's ratio. The Poisson's ratio can be evaluated by the slope of the fitting curves of the experimental data. Here, the averaged PRs of the re-entrant and chiral metamaterials are of -0.59 and -0.92 , respectively. Compared with the design values listed in Table 11, the relative errors are only of 7.81% and 5.15%, respectively, suggesting a good agreement between the experiments and topology-optimized results.

4.3. Thermal expansion experiments

The thermal expansion experiments were conducted by using a self-developed testing setup which was introduced detailly in Ref. [74]. The specimens (Fig. 17(b)) were sprinkled with a random speckle pattern and then were heated by a heating platform from 20 °C up to 60 °C with a specific interval of 10 °C. Through tracking the points extracted from the deformation contours obtained from DIC method, the transverse and longitudinal thermal strains were calculated according to Eqs. (32) and (33). Then, the CTE can be calculated through the slope of the thermal strain versus temperature increment. These tests with the same loading

conditions and measuring method were also repeated for two independent specimens.

As shown in Fig. 18, considering the positive direction of the x and y coordinates in the thermal deformation contours, the speckled areas present the inward displacements. That is the horizontal and vertical shrinkages clearly suggest the expected negative thermal expansions. According to the slope, the averaged CTEs were calculated as shown in Fig. 19. Compared with the design values listed in Table 11, the relative errors of the re-entrant and chiral metamaterials are 17.76% and 15.75%, respectively, revealing that the experimental values match with the topology-optimized results. Coupled with the experimental results of the Poisson's ratio in Section 4.2, the additive manufacturing and experiments for the topological optimized metamaterials demonstrate the effectiveness of the developed AAPO algorithm in this work.

5. Concluding remarks

A systematic development methodology for the multi-functional metamaterials was proposed by developing a multi-material topology optimization and additive manufacturing. A novel heuristic optimization formulation, in which the objective functions would switch dynamically between the loops according to the active phases, was formulated to successfully overcome the convergence oscillation arising from the original Alternating Active Phase algorithm (AAP). The

influences of the controlling parameters in the AAPO algorithm were detailedly discussed, and the appropriate ranges (IterInT:4–6 and IterInP:1–2), which stably provide reasonable designs for all numerical examples, were identified, ensuring the robustness and convergence of the AAPO algorithm.

A series of multi-functional metamaterials (bi-material and tri-material, re-entrant and chiral types), which exclusively realized double negative indexes of Poisson's ratio and thermal expansion, were successfully designed. Especially, the tri-material and chiral metamaterials were obtained through topology optimization for the first time. The numerical simulations of the negative indexes for the metamaterials show considerable consistence with the topology optimized results. The deformation mechanisms of different metamaterials were revealed, as the geometrical feature of the re-entrant and chiral were responsible for the negative Poisson's ratio, while the multi-material layout contributed to the negative thermal expansion. Integrating these two topological characteristics into one kind of metamaterial exactly realize the target multiple functions in this work.

Finally, two types of topology-optimized metamaterials were fabricated by multi-material additive manufacturing using two engineering materials, PVA and nylon. Results of the Poisson's ratio and thermal expansion experiments reveal the well-ordered negative PRs and CTEs. Above experimental validations firmly confirm the validity of the proposed algorithm.

In summary, these multi-material-based development methodologies effectively fills the vacancies in the metamaterial design, which could greatly promote their engineering applications in the aerospace,

electronical and biomedical domains. For dealing with the complex external stimulus, multi-functional metamaterials with different PR and CTE are urgently needed for making both the mechanical- and temperature-sensitive devices such as the deployable antennas and high-precision components in the sensors and actuators. Also, more challenging problems such as the 3D multi-functional metamaterials and the effects of the anisotropy in additive manufacturing could be further explored based on the AAPO algorithm.

CRediT authorship contribution statement

Zhengtong Han: Writing – original draft preparation. **Kai Wei:** Writing – review & editing.

Declaration of Competing Interest

The authors declare that they have no known competing financial interests or personal relationships.

Acknowledgements

This research was supported by the National Natural Science Foundation of China under grant #11972154, and The Science and Technology Innovation Program of Hunan Province under grant #2021RC30306. This research was also supported by the fund of State Key Laboratory of Advanced Design and Manufacturing for Vehicle Body under grant #52175012.

Appendix A. Basic Alternating Active phase algorithm

The AAP algorithm provides a general framework to convert the single material topology optimization into the multi-material one, only requiring the minimal efforts and modifications. A general topology optimization problem is built to clearly express the optimization process of the AAP, in which the objective is to minimize the compliance under the volume fraction constraints. Following the work of Bendsøe and Sigmund [39], the design domain Ω is discretized by finite elements, and the design variables are the relative density of each element, ρ . Let these design variables be combined into a vector, $\boldsymbol{\rho}$. When M different phases of the material are considered, the total number of the solid material is $M-1$ since the void phase is contained. The problem can be mathematically expressed as:

$$\begin{aligned} \min : f(\boldsymbol{\rho}) &= \mathbf{F}^T \mathbf{U} \\ \text{s.t.} : \{ \mathbf{K}(\boldsymbol{\rho}) \mathbf{U} &= \mathbf{F} \quad \sum_{e \in \mathbf{Ne}} \rho_{em} v_e \leq V_m^*, m = 1, \dots, M \quad 0 \leq \rho_{em} \leq 1, e \in \mathbf{Ne}, m = 1, \dots, M \end{aligned} \quad (\text{A1})$$

where $\mathbf{K}(\boldsymbol{\rho})$ is the stiffness matrix obtained by means of finite element discretization. \mathbf{U} and \mathbf{F} are the solution and input vectors, respectively. \mathbf{Ne} is the set of all the elements, and ρ_{em} is the physical density associated with the e th design element with material m . V_m^* is the allowable volume of material m , and v_e is the volume of the e th element.

The schemes for the material interpolation allow intermediate material selection during the solution process. The local material properties are chosen as a local function of the densities of the contributing phases. By penalizing the intermediate densities, the elastic modulus E_e of each element e is given as:

$$E_e(\boldsymbol{\rho}_e) = \sum_{m=1}^M \rho_{em}^p E_m^0 \quad (\text{A2})$$

where E_m^0 is the elastic modulus for material m . Note that the summation of the density variables at each element should be equal to unity:

$$\sum_{m=1}^M \rho_{em} = 1, m = 1, \dots, M, \forall e \in \mathbf{Ne} \quad (\text{A3})$$

In the AAP algorithm, the original problem is converted into a series of binary-phase sub-problems. Therefore, the number of sub-problems is the number of possible combinations ($M(M-1)/2$) of any two phases from a set of M different phases. During the solving process of each subproblem, only two phases are activated at a time when fixing the rest ($M-2$) phases. The updated solution from the current sub-problem is used as the input for the next binary-phase subproblem. As demonstrated in Fig. 19, during the optimization process, let the two active phases be represented by 'a' and 'b', respectively. By using Eq. (A3), the sum of the densities of the two active phases 'a' and 'b' of each element e is:

$$\rho_{ea} + \rho_{eb} = 1 - \sum_{m=1, m \neq a, b}^M \rho_{em} \quad (\text{A4})$$

The problem thus can be simplified by taking the density of one active phase ρ_{ea} as the only design variable. The value of ρ_{eb} is updated by:

$$\rho_{eb} = 1 - \sum_{m=1, m \neq a, b}^M \rho_{em} - \rho_{ea} \tag{A5}$$

The material properties of each element can be calculated through Eq. (A2):

$$E_e(\mathbf{\rho}_e) = \rho_{ea}^p E_a^0 + \rho_{eb}^p E_b^0 + \sum_{m=1, m \neq a, b}^M \rho_{em}^p E_m^0 \tag{A6}$$

According to Eq. (A4), it obtains:

$$E_e(\mathbf{\rho}_e) = \rho_{ea}^p E_a^0 + (r_e - \rho_{ea})^p E_b^0 + \sum_{m=1, m \neq a, b}^M \rho_{em}^p E_m^0 \tag{A7}$$

where

$$r_e = 1 - \sum_{m=1, m \neq a, b}^M \rho_{em}^p \tag{A8}$$

After sensitivity analysis and filtering, the design variables in a sub-problem can be updated through a mature optimizer, i.e., moving asymptotes, convex linearization, and optimality criteria. Compared with a traditional single-material topology optimization method based on the SIMP method, only one additional iterative loop, called as the outer iteration, needs to be added in the algorithm. Although the conversion may increase the computational cost, each binary-phase sub-problem can be solved easily due to fewer design variables and volume constraints. The structure of admissible design domain is very simple such that it is possible to keep optimization iterations strictly feasible, in expense of a negligible computational cost.

(Fig. A1).

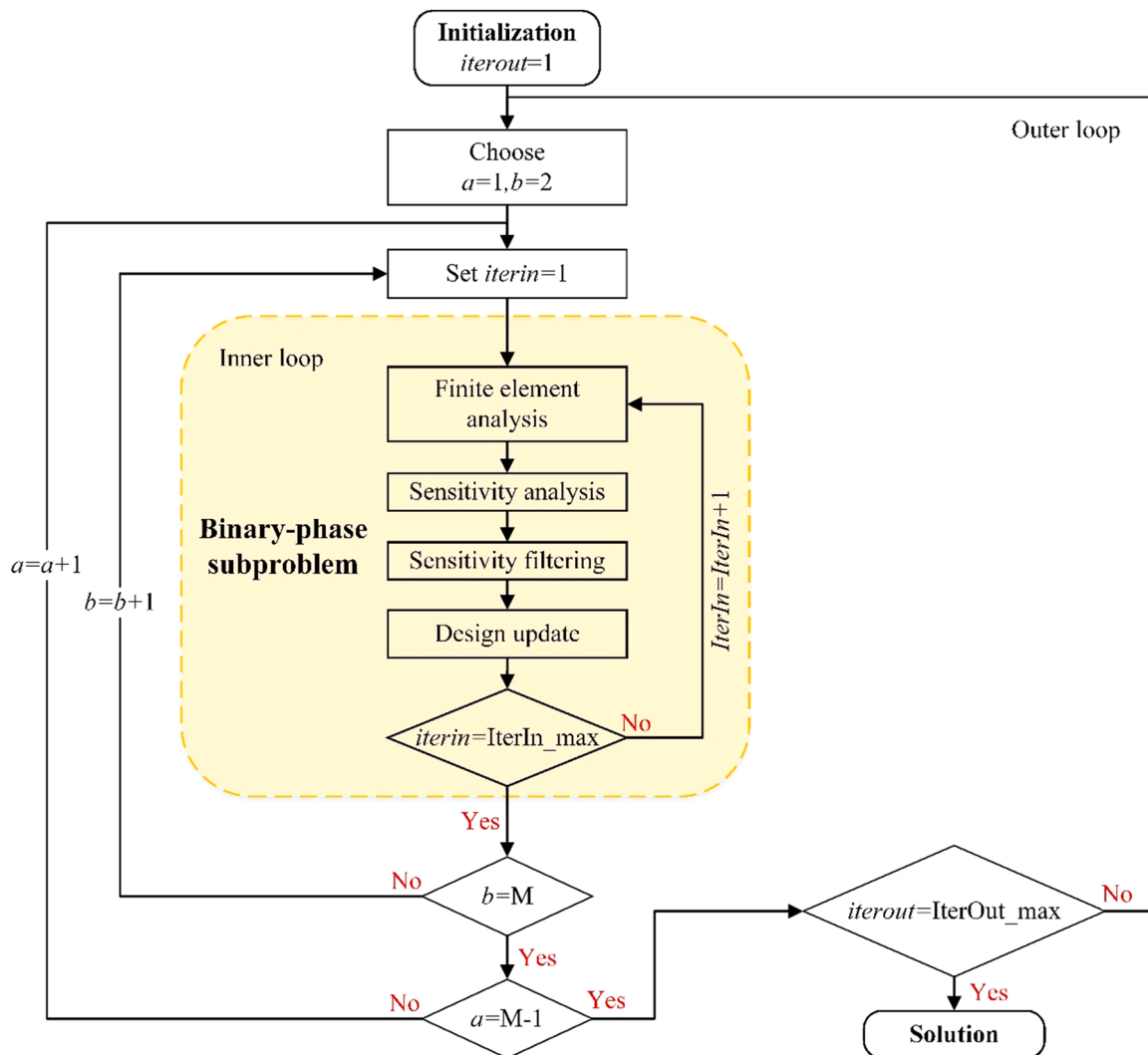


Fig. A1. . Flow chart for the basic Alternating Active Phase algorithm.

Appendix B. Sensitivity analysis of the AAPO algorithm

To use the moving asymptotes (MMA) method to update the iterative design variables, the sensitivity analysis of the objective and constraint functions are analyzed here. Using the material interpolation method introduced in Appendix A, the relationships between the material properties and element densities are established as:

$$\begin{cases} E_e(\boldsymbol{\rho}) = \sum_{m=1}^M \rho_{em}^p E_m^0 \\ \alpha_e(\boldsymbol{\rho}) = \sum_{m=1}^M \rho_{em}^p \alpha_m^0 \end{cases} \tag{A9}$$

where E_m^0 and α_m^0 are the elastic modulus and coefficient of thermal expansion (CTE) for the base material m , respectively. In each subproblem, the material properties for the e th element can thus be simplified as:

$$\begin{cases} E_e(\boldsymbol{\rho}) = \rho_{ea}^p E_a^0 + (r_e - \rho_{ea})^p E_b^0 + \sum_{m=1, m \neq a, b}^M \rho_{em}^p E_m^0 \\ \alpha_e(\boldsymbol{\rho}) = \rho_{ea}^p \alpha_a^0 + (r_e - \rho_{ea})^p \alpha_b^0 + \sum_{m=1, m \neq a, b}^M \rho_{em}^p \alpha_m^0 \end{cases} \tag{A10}$$

For the variable ρ_{ea} , the sensitivities of the homogenized elasticity matrix $\partial C_{ijkl}^H / \partial \rho_{ea}$ are calculated as:

$$\begin{aligned} \frac{\partial C_{ijkl}^H}{\partial \rho_{ea}} &= \frac{1}{|Y|} \int_{Y^e} \frac{\partial C_{pqrs}^e}{\partial \rho_{ea}} \left[\epsilon_{pq}^{0(kl)} - \epsilon_{pq}^*(\chi^{kl}) \right] \left[\epsilon_{rs}^{0(ij)} - \epsilon_{rs}^*(\chi^{ij}) \right] dY^e \\ &+ \frac{2}{|Y|} \int_{Y^e} C_{pqrs}^e \frac{\partial \left[\epsilon_{pq}^{0(kl)} - \epsilon_{pq}^*(\chi^{kl}) \right]}{\partial \rho_{ea}} \left[\epsilon_{rs}^{0(ij)} - \epsilon_{rs}^*(\chi^{ij}) \right] dY^e \end{aligned} \tag{A11}$$

Based on the derivative of Eq., it obtains:

$$\int_Y C_{ijpq} \frac{\partial \left[\epsilon_{pq}^{0(kl)} - \epsilon_{pq}^*(\chi^{kl}) \right]}{\partial \rho_{ea}} \frac{\partial v_i}{\partial y_j} dY = - \int_Y \frac{\partial C_{ijpq}}{\partial \rho_{ea}} \left[\epsilon_{pq}^{0(kl)} - \epsilon_{pq}^*(\chi^{ij}) \right] \frac{\partial v_i}{\partial y_j} dY \tag{A12}$$

Substitute Eq. (A12) into Eq. (A11), it gives:

$$\frac{\partial C_{ijkl}^H}{\partial \rho_{ea}} = - \frac{1}{|Y|} \int_{Y^e} \frac{\partial C_{pqrs}^e}{\partial \rho_{ea}} \left[\epsilon_{pq}^{0(kl)} - \epsilon_{pq}^*(\chi^{kl}) \right] \left[\epsilon_{rs}^{0(ij)} - \epsilon_{rs}^*(\chi^{ij}) \right] dY^e \tag{A13}$$

Similarly, the sensitivities of the homogenized thermal stress vector $\partial \beta_{pq}^H / \partial \rho_{ea}$ can also be calculated as:

$$\begin{aligned} \frac{\partial \beta_{pq}^H}{\partial \rho_{ea}} &= - \frac{1}{|Y|} \int_{Y^e} \frac{\partial C_{pqrs}^e}{\partial \rho_{ea}} \left[\alpha_{pq} - \epsilon_{pq}^*(\psi) \right] \left[\epsilon_{rs}^{0(ij)} - \epsilon_{rs}^*(\chi^{kl}) \right] dY^e \\ &+ \frac{1}{|Y|} \int_{Y^e} C_{pqkl}^e \frac{\partial \alpha_{pq}^e}{\partial \rho_{ea}} \left[\epsilon_{kl}^{0(ij)} - \epsilon_{kl}^*(\chi^{ij}) \right] dY^e \end{aligned} \tag{A14}$$

The derivations of the matrix C_{pqrs}^e and α_{pq}^e respected to the design variables can be deduced by using the interpolation model in Eq. (A10):

$$\frac{\partial C_{pqrs}^e}{\partial \rho_{ea}} = p \rho_{ea}^{p-1} E_a^0 + p (r_e - \rho_{ea})^{p-1} E_b^0 + \sum_{m=1, m \neq a, b}^M \rho_{em}^p E_m^0 \tag{A15}$$

$$\frac{\partial \alpha_{pq}^e}{\partial \rho_{ea}} = p \rho_{ea}^{p-1} \alpha_a^0 + p (r_e - \rho_{ea})^{p-1} \alpha_b^0 + \sum_{m=1, m \neq a, b}^M \rho_{em}^p \alpha_m^0 \tag{A16}$$

Then the derivative of the CTE vector with respect to the design variables is:

$$\frac{\partial \alpha_{ij}^H}{\partial \rho_{ea}} = \frac{\partial \left(C_{ijkl}^H \right)^{-1}}{\partial \rho_{ea}} \beta_{kl}^H + \left(C_{ijkl}^H \right)^{-1} \frac{\partial \beta_{kl}^H}{\partial \rho_{ea}} \tag{A17}$$

Thus, the derivatives of the objective functions in Eq. and with respect to the design variables are expressed as:

$$\frac{\partial f_t}{\partial \rho_{ea}} = \frac{\partial f_t}{\partial \alpha_{ij}^H} \frac{\partial \alpha_{ij}^H}{\partial \rho_{ea}}, e = 1, 2, \dots, N \tag{A18}$$

$$\frac{\partial f_p}{\partial \rho_{ea}} = \frac{\partial f_p}{\partial C_{ijkl}^H} \frac{\partial C_{ijkl}^H}{\partial \rho_{ea}}, e = 1, 2, \dots, N \tag{A19}$$

where N represents the number of the variables. The constraints in the optimization problem can be written as:

$$f_v(\boldsymbol{\rho}) = \frac{\sum_{e=1}^N \rho_{ea} v_e}{V} \leq V_a^* \quad (\text{A20})$$

where v_e and V are the volume of the e th element and all elements, respectively. V_a^* is the volume constraint of the material 'a'. Similarly, the derivative of the volume constraint can also be obtained as $\partial f_v / \partial \rho_{ea} = v_e / V$.

References

- [1] R. Lakes, Foam structures with a negative Poisson's ratio, *Science* 235 (1987) 1038–1041.
- [2] R. Gatt, J.N. Grima, Negative compressibility, *Phys. Status Solidi (RRL)*, *Phys. Status Solidi* 2 (2008) 236–238.
- [3] Z.G. Nicolaou, A.E. Motter, Mechanical metamaterials with negative compressibility transitions, *Nat. Mater.* 11 (7) (2012) 608–613.
- [4] W. Miller, C. Smith, D. Mackenzie, K. Evans, Negative thermal expansion: a review, *J. Mater. Sci.* 44 (20) (2009) 5441–5451.
- [5] X. Yu, J. Zhou, H. Liang, Z. Jiang, L. Wu, Mechanical metamaterials associated with stiffness, rigidity and compressibility: a brief review, *Prog. Mater. Sci.* 94 (2018) 114–173.
- [6] E. Pasternak, A.V. Dyskin, Materials and structures with macroscopic negative Poisson's ratio, *Int. J. Eng. Sci.* 52 (2012) 103–114.
- [7] J. Choi, R. Lakes, Fracture toughness of re-entrant foam materials with a negative Poisson's ratio: experiment and analysis, *Int. J. Fract.* 80 (1) (1996) 73–83.
- [8] C. Chen, R. Lakes, Micromechanical analysis of dynamic behavior of conventional and negative Poisson's ratio foams, (1996) 67–80.
- [9] L. Ai, X.L. Gao, An analytical model for star-shaped re-entrant lattice structures with the orthotropic symmetry and negative Poisson's ratios, *Int. J. Mech. Sci.* 145 (2018) 158–170.
- [10] J.N. Grima, R. Gatt, A. Alderson, K.E. Evans, On the potential of connected stars as auxetic systems, *Mol. Simula* 31 (13) (2005) 925–935.
- [11] B. Ling, K. Wei, Z. Qu, D. Fang, Design and analysis for large magnitudes of programmable Poisson's ratio in a series of lightweight cylindrical metastructures, *Int. J. Mech. Sci.* 195 (2021), 106220.
- [12] D. Prall, R. Lakes, Properties of a chiral honeycomb with a Poisson's ratio of -1, *Int. J. Mech. Sci.* 39 (3) (1997) 305–314.
- [13] C.W. Smith, J. Grima, K. Evans, A novel mechanism for generating auxetic behaviour in reticulated foams: missing rib foam model, *Acta Mater.* 48 (17) (2000) 4349–4356.
- [14] A. Alderson, K.L. Alderson, D. Attard, K.E. Evans, R. Gatt, J.N. Grima, W. Miller, N. Ravirala, C. Smith, K. Zied, Elastic constants of 3-, 4- and 6-connected chiral and anti-chiral honeycombs subject to uniaxial in-plane loading, *Compos. Sci. Technol.* 70 (7) (2010) 1042–1048.
- [15] J. Dirrenberger, S. Forest, D. Jeulin, C. Colin, Homogenization of periodic auxetic materials, 2011 21–26.
- [16] K. Wei, Y. Peng, Z. Qu, Y. Pei, D. Fang, A cellular metastructure incorporating coupled negative thermal expansion and negative Poisson's ratio, *Int. J. Solids Struct.* 150 (2018) 255–267.
- [17] G. Jefferson, T.A. Parthasarathy, R.J. Kerans, Tailorable thermal expansion hybrid structures, *Int. J. Solids Struct.* 46 (11–12) (2009) 2372–2387.
- [18] E.M. Parsons, Lightweight cellular metal composites with zero and tunable thermal expansion enabled by ultrasonic additive manufacturing: Modeling, manufacturing, and testing, *Compos. Struct.* 223 (2019), 110656.
- [19] J. Qu, M. Kadic, A. Naber, M. Wegener, Micro-structured two-component 3D metamaterials with negative thermal-expansion coefficient from positive constituents, *Sci. Rep.* 7 (1) (2017) 1–8.
- [20] Q. Wang, J.A. Jackson, Q. Ge, J.B. Hopkins, C.M. Spadaccini, N.X. Fang, Lightweight mechanical metamaterials with tunable negative thermal expansion, *Phys. Rev. Lett.* 117 (17) (2016), 175901.
- [21] M.M. Toropova, C.A. Steeves, Adaptive bimaterial lattices to mitigate thermal expansion mismatch stresses in satellite structures, *Acta Astronaut.* 113 (2015) 132–141.
- [22] K. Wei, H. Chen, Y. Pei, D. Fang, Planar lattices with tailorable coefficient of thermal expansion and high stiffness based on dual-material triangle unit, *J. Mech. Phys. Solids* 86 (2016) 173–191.
- [23] H. Xu, D. Pasini, Structurally efficient three-dimensional metamaterials with controllable thermal expansion, *Sci. Rep.* 6 (1) (2016) 1–8.
- [24] R.L. Lincoln, F. Scarpa, V.P. Ting, R.S. Trask, Multifunctional composites: a metamaterial perspective, *Multifunct. Mater.* 2 (4) (2019), 043001.
- [25] C. Huang, L. Chen, Negative Poisson's ratio in modern functional materials, *Adv. Mater.* 28 (37) (2016) 8079–8096.
- [26] K. Wei, H. Chen, Y. Pei, D. Fang, Planar lattices with tailorable coefficient of thermal expansion and high stiffness based on dual-material triangle unit, *J. Mech. Phys. Solids* 86 (2016) 173–191.
- [27] X. Li, L. Gao, W. Zhou, Y. Wang, Novel 2D metamaterials with negative Poisson's ratio and negative thermal expansion, *Extrem. Mech. Lett.* 30 (2019), 100498.
- [28] M.M. Chen, M.H. Fu, Lin Hua, S.V. Sheshenin, A novel 3D structure with tunable Poisson's ratio and tailorable coefficient of thermal expansion based on a tri-material triangle unit, *Compos. Struct.* (2020), 112803.
- [29] X.L. Peng, S. Bargmann, A novel hybrid-honeycomb structure: enhanced stiffness, tunable auxeticity and negative thermal expansion, *Int. J. Mech. Sci.* (2020), 106021.
- [30] B.B. Zheng, M.H. Fu, W.H. Li, L.L. Hu, A novel re-entrant honeycomb of negative thermal expansion, *Smart. Mater. Struct.* 27 (8) (2018), 085005.
- [31] L. Ai, X.L. Gao, Three-dimensional metamaterials with a negative Poisson's ratio and a non-positive coefficient of thermal expansion, *Int. J. Mech. Sci.* 135 (2018) 101–113.
- [32] C.S. Ha, E. Hestekin, J. Li, M.E. Plesha, R.S. Lakes, Controllable thermal expansion of large magnitude in chiral negative Poisson's ratio lattices, *Phys. Status Solidi (b)* 252 (7) (2015) 1431–1434.
- [33] L. Wu, B. Li, J. Zhou, Isotropic negative thermal expansion metamaterials, *ACS Appl. Mater. Interfaces* 8 (27) (2016) 17721–17727.
- [34] H. Yu, W. Wu, J. Zhang, J. Chen, H. Liao, D. Fang, Drastic tailorable thermal expansion chiral planar and cylindrical shell structures explored with finite element simulation, *Compos. Struct.* 210 (2019) 327–338.
- [35] M. Fu, J. Huang, B. Zheng, Y. Chen, C. Huang, Three-dimensional auxetic materials with controllable thermal expansion, *Smart. Mater. Struct.* 29 (8) (2020), 085034.
- [36] P. Vogiatzis, S. Chen, X. Wang, T. Li, L. Wang, Topology optimization of multi-material negative Poisson's ratio metamaterials using a reconciled level set method, *Comput. Aided Des.* 83 (2017) 15–32.
- [37] O. Sigmund, K. Maute, Topology optimization approaches, *Struct. Multidiscip. O* 48 (6) (2013) 1031–1055.
- [38] M. Osanov, J.K. Guest, Topology optimization for architected materials design, *Annu. Rev. Mater. Res.* 46 (2016) 211–233.
- [39] M.P. Bendsoe, O. Sigmund, Material interpolation schemes in topology optimization, *Arch. Appl. Mech.* 69 (9) (1999) 635–654.
- [40] L. Yin, G. Ananthasuresh, Topology optimization of compliant mechanisms with multiple materials using a peak function material interpolation scheme, *Struct. Multidiscip. Optim.* 23 (1) (2001) 49–62.
- [41] R. Tavakoli, S.M. Mohseni, Alternating active-phase algorithm for multimaterial topology optimization problems: a 115-line MATLAB implementation, *Struct. Multidiscip. Optim.* 49 (4) (2014) 621–642.
- [42] W. Zuo, K. Saitou, Multi-material topology optimization using ordered SIMP interpolation, *Struct. Multidiscip. Optim.* 55 (2) (2017) 477–491.
- [43] K. Long, X. Wang, X. Gu, Local optimum in multi-material topology optimization and solution by reciprocal variables, *Struct. Multidiscip. Optim.* 57 (3) (2018) 1283–1295.
- [44] X. Huang, Y.M. Xie, Bi-directional evolutionary topology optimization of continuum structures with one or multiple materials, *Comput. Mech.* 43 (3) (2009) 393.
- [45] K. Ghabraie, An improved soft-kill BESO algorithm for optimal distribution of single or multiple material phases, *Struct. Multidiscip. Optim.* 52 (4) (2015) 773–790.
- [46] M.Y. Wang, X. Wang, "Color" level sets: a multi-phase method for structural topology optimization with multiple materials, *Comput. Method. Appl. Method* 193 (6–8) (2004) 469–496.
- [47] A. Ramani, A pseudo-sensitivity based discrete-variable approach to structural topology optimization with multiple materials, *Struct. Multidiscip. Optim.* 41 (6) (2010) 913–934.
- [48] E.D. Sanders, M.A. Aguiló, G.H. Paulino, Multi-material continuum topology optimization with arbitrary volume and mass constraints, *Comput. Method. Appl. Method* 340 (2018) 798–823.
- [49] O. Sigmund, Tailoring materials with prescribed elastic properties, *Mech. Mater.* 20 (4) (1995) 351–368.
- [50] H. Zhang, Y. Luo, Z. Kang, Bi-material microstructural design of chiral auxetic metamaterials using topology optimization, *Compos. Struct.* 195 (2018) 232–248.
- [51] G. Zhang, K. Khandelwal, Computational design of finite strain auxetic metamaterials via topology optimization and nonlinear homogenization, *Comput. Method. Appl. Method* 356 (2019) 490–527.
- [52] J. Gao, H. Xue, L. Gao, Z. Luo, Topology optimization for auxetic metamaterials based on isogeometric analysis, *Comput. Method. Appl. M* 352 (2019) 211–236.
- [53] O. Sigmund, S. Torquato, Composites with extremal thermal expansion coefficients, *Appl. Phys. Lett.* 69 (21) (1996) 3203–3205.
- [54] E. Andreassen, C.S. Andreasen, How to determine composite material properties using numerical homogenization, *Comp. Mater. Sci.* 83 (2014) 488–495.
- [55] Z. Han, K. Wei, Z. Gu, X. Ma, X. Yang, Stress-constrained multi-material topology optimization via an improved alternating active-phase algorithm, *Eng. Optim.* (2021) 1–24.
- [56] M. Hirota, Y. Kanno, Optimal design of periodic frame structures with negative thermal expansion via mixed integer programming, *Optim. Eng.* 16 (4) (2015) 767–809.

- [57] A. Takezawa, M. Kobashi, Design methodology for porous composites with tunable thermal expansion produced by multi-material topology optimization and additive manufacturing, *Compos. Part. B Eng.* 131 (2017) 21–29.
- [58] Y. Wang, J. Gao, Z. Luo, T. Brown, N. Zhang, Level-set topology optimization for multimaterial and multifunctional mechanical metamaterials, *Eng. Optim.* 49 (1) (2017) 22–42.
- [59] M. Cui, H. Chen, J. Zhou, F. Wang, A meshless method for multi-material topology optimization based on the alternating active-phase algorithm, *Eng. Comput.* 33 (4) (2017) 871–884.
- [60] Q.X. Lieu, J. Lee, A multi-resolution approach for multi-material topology optimization based on isogeometric analysis, *Comput. Method. Appl. Mech.* 323 (2017) 272–302.
- [61] W. Sha, M. Xiao, L. Gao, Y. Zhang, A new level set based multi-material topology optimization method using alternating active-phase algorithm, *Comput. Method. Appl. Mech.* 377 (2021), 113674.
- [62] J. Park, A. Sutradhar, A multi-resolution method for 3D multi-material topology optimization, *Comput. Method. Appl. Mech.* 285 (2015) 571–586.
- [63] B. Majidi, A. Reza, Multi-material topology optimization of compliant mechanisms via solid isotropic material with penalization approach and alternating active phase algorithm, *Proc. Inst. Mech. Eng., P. I. Mech. Eng. C. J. Mech.* 234 (13) (2020) 2631–2642.
- [64] S. Watts, D.A. Tortorelli, Optimality of thermal expansion bounds in three dimensions, *Extrem. Mech. Lett.* 12 (2017) 97–100.
- [65] R.T. Marler, J.S. Arora, Survey of multi-objective optimization methods for engineering, *Struct. Multidiscip. Optim.* 26 (6) (2004) 369–395.
- [66] O. Sigmund, Materials with prescribed constitutive parameters: an inverse homogenization problem, *Int. J. Solids Struct.* 31 (17) (1994) 2313–2329.
- [67] J. Gao, M. Xiao, L. Gao, J. Yan, W. Yan, Isogeometric topology optimization for computational design of re-entrant and chiral auxetic composites, *Comput. Method. Appl. Mech.* 362 (2020), 112876.
- [68] J. Wu, Z. Luo, H. Li, N. Zhang, Level-set topology optimization for mechanical metamaterials under hybrid uncertainties, *Comput. Method. Appl. Mech.* 319 (2017) 414–441.
- [69] Y. Wang, Z. Luo, N. Zhang, Z. Kang, Topological shape optimization of microstructural metamaterials using a level set method, *Comp. Mater. Sci.* 87 (2014) 178–186.
- [70] A.M. Mirzendehtel, K. Suresh, A. Pareto-optimal, approach to multimaterial topology optimization, *J. Mech. Des.* 137 (10) (2015).
- [71] N. Xu, H.T. Liu, M.R. An, L. Wang, Novel 2D star-shaped honeycombs with enhanced effective Young's modulus and negative Poisson's ratio, *Extrem. Mech. Lett.* 43 (2021), 101164.
- [72] L. Ai, X.L. Gao, Metamaterials with negative Poisson's ratio and non-positive thermal expansion, *Compos. Struct.* 162 (2017) 70–84.
- [73] C.K. Ng, K.K. Saxena, R. Das, E.I.S. Flores, On the anisotropic and negative thermal expansion from dual-material re-entrant-type cellular metamaterials, *J. Mater. Sci.* 52 (2) (2016) 1–14.
- [74] K. Wei, X. Xiao, J. Chen, Y. Wu, M. Li, Z. Wang, Additively manufactured bi-material metamaterial to program a wide range of thermal expansion, *Mater. Des.* 198 (2021), 109343.
- [75] M.Z. Siddiqui, F. Tariq, N. Naz, Application of a two-step digital image correlation algorithm in determining Poisson's ratio of metals and composites, 62nd International Astronautical Congress, Materials and Structures Symposium Cape Town, 2011, 15434.